Politecnico di Milano

Dipartimento di Fisica

Ph.D. Dissertation in Physics

A novel photodetector platform based on Ge and Si microcrystals for VIS-NIR detection

Virginia Falcone

XXXV Ph.D. cycle in Physics

Supervisor:
Prof. Giovanni Isella
Tutor:
Prof. Franco Ciccacci

Academic Year 2022/2023

Abstract

In this work, we devise a new type of photodetector based on Si and Ge-on-Si 3D self-assembled microcrystals. To this aim, we searched for the optimal growth parameters (doping profile and thickness) to reach a desired profile of the electric field inside the microcrystals. More specifically I developed a Finite Difference Time Domain simulation predicting an enhancement in the fraction of absorbed light of these microcrystals compared to planar epilayers. I experimentally demonstrated such enhancement by responsivity measurements. Simulations and experimental results nicely agrees both for single microcrystals and for devices based on microcrystal arrays. Finally, I have investigated the operation of the Si microcrystals as Avalanche PhotoDiodes (APDs) and Single Photon Avalanche Diodes (SPADs). Notably, the gain obtained in the APDs reaches a maximum value comparable to state-of-the-art commercial devices, while the SPAD measurements point towards the exploitation of Si microcrystals even as single photon detectors.

Contents

List of Figures **5**

Introduction **7**

1 Semiconductor based photodetectors **11**
- 1.1 Semiconductor-based photodetectors 11
- 1.2 Avalanche photodiode 15
- 1.3 Single photon avalanche diode 18

2 3D microcrystals **21**
- 2.1 3D self-assembled microcrystal 21
- 2.2 LEPECVD growth 22
- 2.3 Modelling of microcrystal growth 24
  - 2.3.1 Microcrystals defects 28
- 2.4 Electronic and optical modelling 29
  - 2.4.1 Electronic modelling 29
  - 2.4.2 Optical modelling 30

3 Ge/Si microcrystals **33**
- 3.1 Photodetection with Ge/Si self-assembled microcrystal 33
  - 3.1.1 FDTD modelling of Ge/Si microcrystals 34
  - 3.1.2 Electro-optical characterization of a single Ge/Si microcrystal 37
- 3.2 Photodetectors based on Ge/Si microcrystal arrays 40
  - 3.2.1 Fabrication process 40
  - 3.2.2 Electro-optical characterization of the device 43

4 Si microcrystals as a photodetection platform **49**
- 4.1 Optical simulation of Si microcrystals 49
- 4.2 Electrical properties of Si microcrystals 50
- 4.3 Electro-optical characterization of a single Si microcrystal 52
- 4.4 Implanted Si microcrystal as avalanche photodiodes 55
- 4.5 Implanted Si microcrystal as single photon avalanche diodes . . . 56

Conclusion **65**

A Additional data **67**

Appendix **67**
A.1 FDTD simulations of Ge/Si microcrystal 67
A.2 Responsivity dependence on morphology for single Ge/Si microcrystal 68
A.3 NEP and specific detectivity of implanted Si microcrystal 69

Bibliography **71**

List of Figures

1 Absorption coefficient of silicon and germanium 8

1.1 Photodetector devices 12
1.2 Band diagram of a Ge *p*-*i*-*n* junction 12
1.3 IV curve of a *p*-*i*-*n* junction under dark condition 13
1.4 Basic principle of the avalanche regime 15
1.5 Estimation of the multiplication factor 17
1.6 The three phases of SPAD operation 18
1.7 Gated-mode operation 19

2.1 SEM images of pre-patterned Si substrate and 3D Ge microcrystals 22
2.2 Table of the Si pattern geometries 23
2.3 Sketch of a CVD chamber 23
2.4 Sketch of a LEPECVD reactor 24
2.5 SEM image of 3D self-assembled microcrystals 25
2.6 Table of the patterns used for device fabrication 25
2.7 Representation of the degree of faceting of the patterns 26
2.8 Borgstrom construction 27
2.9 Growth profile of the microcrystals 28
2.10 TEM analysis of a Si microcrystal 29
2.11 TEM analysis of Ge microcrystals 30
2.12 Doping profile of Ge and Si microcrystals 31
2.13 Electronic simulation 32
2.14 Optical simulation 32

3.1 SEM images of Ge patterns 34
3.2 Sketches of Ge FDTD simulations 35
3.3 Result of Ge FDTD simulations: A, C, O and Ge epilayer 35
3.4 Result of Ge FDTD simulations: ratio between C and Ge epilayer 36
3.5 FDTD simulations for different periodicities 36
3.6 Experimental setup 37
3.7 Ge IV curve 38
3.8 Normalized Responsivity of the microcrystals G and O 39
3.9 Responsivity of Ge microcrystal and a Ge mesa diode 39
3.10 NEP of a single Ge microcrystal 40
3.11 Fabrication process of Ge patterns 41
3.12 SEM image of a single layer of graphene on a microcrystal array 42
3.13 SEM images of the Ge device 42
3.14 Responsivity of the final device of Ge microcrystals array 43

3.15 Comparison between the responsivity of three different patterns . 44
3.16 Responsivity of the Ge planar device 45
3.17 Comparison between the responsivity of the Gr/Ge microcrystal device and the responsivity of the Ge planar device 45
3.18 η_{ex} of post-growth microcrystal and of the final device 46
3.19 η_{ex} as function of the ratio between the absorbing layer thickness and the diffusion length 46
3.20 η_{ex} in the wavelength range from 1300 to 1700 nm, for different thickness of the absorbing layer 47

4.1 FDTD simulation for a Si planar epilayer and a Si microcrystal . 50
4.2 Doping profiles of the Si microcrystals 51
4.3 Electrical simulations for the in-situ doped Si microcrystal 51
4.4 Electrical simulations for the implanted Si microcrystal 52
4.5 IV curve of single Si microcrystals 53
4.6 Top-view SEM images of pattern K and N 53
4.7 Responsivity for pattern K and N 54
4.8 Sketch of the Si mesa diode and its responsivity 54
4.9 Comparison between the normalized responsivities of the microcrystals and the fabricated Si mesa-diode 55
4.10 Experimental gain for pattern K and N 56
4.11 Fitting of the experimental gain for pattern N 57
4.12 Sketches of the fabrication process based on photoresist filling and ITO as top transparent contact 58
4.13 SEM images of the photoresist filling and the ITO deposition . . 58
4.14 SEM images of holes in the photoresist filling 59
4.15 Sketches of the fabrication process based on SiO_2 deposition and planarization, and metal as top contact 60
4.16 Dark and illuminated IV curve of the metal device based on Si microcrystals 61
4.17 Dark and illuminated IV curve of the ITO device based on Si microcrystals 62
4.18 Comparison between the responsivity of the ITO device and the metal one 62
4.19 Real time response of the metal device in gated-mode 63

A.1 Result of Ge FDTD simulations: ratio between A, O and Ge epilayer 67
A.2 Geometric characteristics and degree of faceting of the pattern C and I 68
A.3 Comparison between the normalized responsivity of the pattern C and I 68
A.4 NEP and D^* of implanted Si microcrystal 69

Introduction

The use of semiconductors in electronics and integrated optics has increased during the last years, requiring the development of more performing devices. For more than 50 years silicon has been the workhorse of the information revolution, however, more recently other semiconducting materials, such as germanium, have been added to the CMOS portfolio, improving or adding novel functionalities to Si-based technology.

One of the major applications of such semiconductors is photodetection for a variety of applications as imaging [1], telecommunications and single photon detection. The choice of the semiconductor defines the spectral range of the photodetector. Fig 1 shows the absorption coefficient as a function of the wavelength of silicon and germanium.

The direct epitaxial growth of silicon and germanium on silicon (Ge-on-Si) has fostered the development of visible-near-infrared detectors. Silicon-based devices allow photodetection from 500 up to 1100 nm, covering the VIS and NIR range, exploiting the absorption at the indirect gap at 1.12 eV. Instead, those based on germanium can theoretically work in the Short-Wave InfraRed (SWIR) range from 1200 to 1800 nm, using both the absorption at the direct (0.8 eV) and the indirect gap (0.66 eV). However, the absorption coefficient of germanium at the indirect gap is so low that conventional Ge-on-Si *p-i-n* photodetectors features a negligibly small responsivity above 1550 nm. To overcome this problem a several micrometers thick absorbing layer is required, increasing the risk of generating cracks and wafer bowing. A viable route to enhance the responsivity of Si and Ge-on-Si photodetectors, in particular in the spectral region from 1550 to 1800 nm, might be exploiting the micro-structuring of the absorbing layer to increase the effective volume of interaction between light and matter.

In this work I report on a new type of detectors, obtained from Si and Ge microcrystals epitaxially grown on a patterned Si substrate [2,3]. The novelty of this research starts from the epitaxial growth of this particular structure. In addition, a dedicated electronic modelling has been performed to optimize the doping profile of the microcrystals ensuring their operation as linear photodetectors or avalanche photodiodes.

The modelling of the visible-IR absorption properties of the Si and Ge-on-Si microcrystals has been performed by Finite Difference Time Domain (FDTD) simulations [4,5]. The faceted morphology and relatively high aspect ratio of the microcrystals is seen to enhance the fraction of absorbed light and the detector responsivity in the wavelength region of the indirect regime of absorption, as compared to conventional planar devices. This, in particular for the germanium, admits the possibility to extent the responsivity up to 1800 nm.

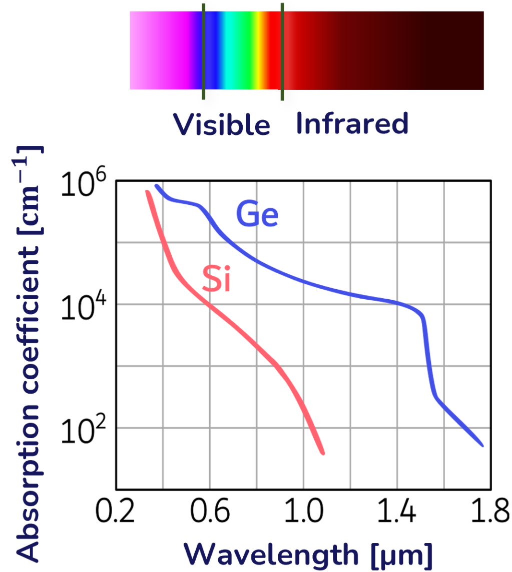

Figure 1: Absorption coefficient as a function of wavelength: silicon (red line) and germanium (blue line).

The main challenge in realizing vertically illuminated photodiodes based on microcrystals is the formation of a top transparent contact that can adapt to the surface morphology and bridge the 100-200 nm gap between adjacent microcrystals. To this purpose, different fabrication processes have been developed using transparent conductive oxide or graphene as a suspended continuous top contact. The optical properties of Si-Ge microcrystals make them promising building blocks for optoelectronic devices operating in the VIS-NIR spectral region.

In this work, each step from the growth to the final fabrication process of Si-Ge microcrystal will be analyzed.

Chapter 1 describes the theory underlying the detection process in semiconductor devices, with a focus on avalanche photodiodes and single photon avalanche diodes.

Chapter 2 reports on the microcrystal growth process and on their electronic/optical properties. The first part describes the LEPECVD growth technique used to generate such 3D microcrystals, while the second part addresses the electronic and optical simulations used to model the electro-optical properties of the 3D microcrystals.

Chapter 3 presents the electro-optical properties of individual Ge microcrystals and of a photodetector obtained using graphene to contact a microcrystals array.

The first part of chapter 4 is devoted to the electro-optical characterization of single Si microcrystals (operating as a linear photodetector and as a avalanche photodiode). In the second part I describe two different fabrication

process developed to characterize the Si microcrystal response as single photon avalanche diode. Finally, preliminary results on the microcrystal based single photon avalanche diode are reported.

Chapter 1

Semiconductor based photodetectors

In the first chapter the working principle of semiconductor-based photodetection devices is introduced. Linear photodetectors, giving a photocurrent proportional to the photon flux are the most commonly used (1.1). For specific semiconductors there is also the possibility to achieve an internal gain as in the case for avalanche photodiodes (APDs) or single photon avalanche diodes (SPADs) as we will see in 1.2, for the first, and 1.3 for the second case.

1.1 Semiconductor-based photodetectors **11**
1.2 Avalanche photodiode **15**
1.3 Single photon avalanche diode **18**

1.1 Semiconductor-based photodetectors

A photodetector exploits the generation of electron-hole pairs due to the absorption of photons with energy higher than the energy gap of the semiconductor. The separation of the generated electron-hole pair, can be obtaines either by applying an external electric field to a semiconductor layer or by means an intrinsic electric field present in the material, as in the case of a *p*-*i*-*n* junction. In the first case at the right and left side of the semiconductor two contact layers are present as in Fig 1.1 (a), realizing a Metal-Semiconductor-Metal (MSM) photodetector. Under dark conditions a bias applied to the two electrodes will give rise to the so called dark current. Under illumination, maintaining the same applied bias, a photocurrent is generated in addition to the dark current thanks to the collection of the photogenerated electron-hole pairs. Therefore the final measured current under illumination will be given by the sum of the dark current and the photocurrent.

The structure of a photodetector based on a *p*-*i*-*n* junction is sketched in Fig 1.1 (b). The junction formed between the *p*-doped, intrinsic and *n*-doped layers leads to a band bending with a consequent potential drop, called built-in potential (see Fig 1.2). In the case of an highly intrinsic i-layer the depleted

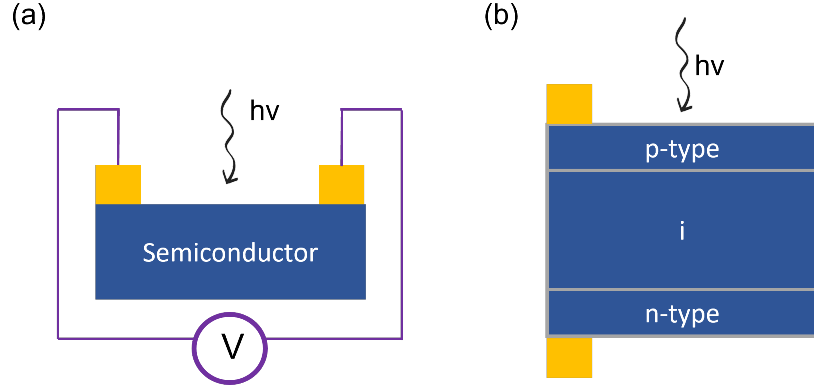

Figure 1.1: (a) MSM operating as photodetector by the application of an external electric field at the metallic contacts; (b) *p*-*i*-*n* photodetector.

region will coincide with the i-region (see Fig 1.2(a)). In case the nominally intrinsic region features some residual doping, a depleted layer will form at the interface between the i-layer and one of the two contacts. Fig 1.2(b) shows the band diagram in the case of a residual p-type doping within the (nominally) i-layer. Thereby the absorption of photons with $h\nu \geq E_g$ will take place mainly in the intrinsic/depleted region. The generated electron, as a result of the intrinsic electric field of the junction, will move towards the *n*-doping region while the hole towards the *p*-doped one. In this way, by means of the top/back contact and an external circuit, it will be possible to collect the dark current and the final photocurrent signal.

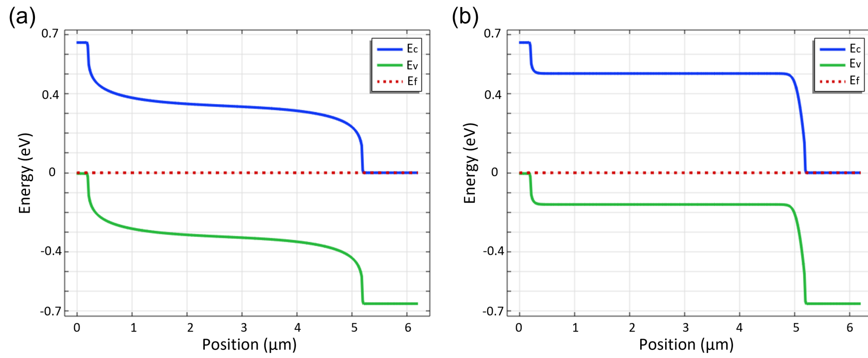

Figure 1.2: Band diagram of a Ge *p*-*i*-*n* junction: (a) 200 nm of p^+ top contact (5×10^{18}cm^{-3}), 5μm of highly intrinsic layer (n=p=2×10^{13}cm^{-3}) and 1μm of n^+ (1×10^{19}cm^{-3}); (b) 200 nm of p^+ top contact (5×10^{18}cm^{-3}), 5μm of intrinsic layer with residual *p*-type doping (1×10^{16}cm^{-3}) and 1μm of n^+ (1×10^{19}cm^{-3}).

The IV curve, under dark condition, for a *p*-*i*-*n* photodetectors will present a rectifying behaviour (Fig 1.3). For forward applied bias, positive at the *p*-type contact, a reduction of the barrier for the holes and electrons occurs with a high exponential increase of the current. Instead for reverse bias, negative at the

p-type contact, an increase of the barrier both for electrons and holes will imply a strong reduction of the current flow with a final low value of dark current.

This photodiode typically operates in reverse bias regime with an external bias applied in addition to the built-in potential. By knowing the carrier density along the z axis of the junction, it is possible to calculate the electric field $E(z)$ and consequently also of the potential $V(z)$ by means of the Poisson equation.

$$\frac{d^2V}{dz^2} = \frac{\rho(z)}{\epsilon} \tag{1.1}$$

Beside photogeneration, there are also non-radiative generation mechanisms such as, diffusion, band-to-band thermal generation, trap assisted generation and trap assisted tunnelling. This type of non-radiative generation-recombination mechanisms will contribute to the photodetector's dark current. In particular, their contribution will be greater for semiconductors with a small energy gap (germanium) as compared to semiconductor with a larger bandgap (silicon).

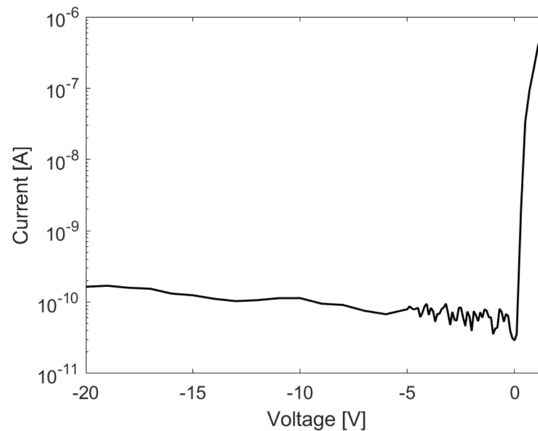

Figure 1.3: Rectifying behaviour of a p-i-n photodetector.

The main parameters that determine the performance of a photodetector are: responsivity, quantum efficiency, collection efficiency, Noise Equivalent Power (NEP) and detectivity [6]. The responsivity is defined as the ratio between the photocurrent and the incident power ($Resp = I_{ph}/P$). The latter can be expressed as a function of the flux of incident photons Φ as:

$$P = \frac{\Phi\, hc}{\lambda} \tag{1.2}$$

with h Planck's constant, λ wavelength and c the speed of light.

Another important parameter is the external quantum efficiency η_{ex} defined as the ratio between the electron flow in the external read-out circuit and the photon flux impinging on the detector:

$$\eta_{ex} = \frac{I_{ph}}{q\,\Phi} \tag{1.3}$$

where q is the electron charge. The fraction of photons not reflected at the photodetector surface is given by $(1 - R)$ being R the surface reflectance that, for normal incidence and neglecting internal reflection effects can be expressed as:

$$R = \frac{(n-1)^2 + \kappa^2}{(n+1)^2 + \kappa^2} \tag{1.4}$$

where n and κ area real and imaginary components of the refractive index.

Each photon crossing the device has a probability η_q of being absorbed. In its simplest form η_q can be expressed as:

$$\eta_q = 1 - e^{-\alpha\, d} \tag{1.5}$$

being α and d the absorption coefficient and device thickness, respectively.

Only a fraction η_c of the photogenerated electron-hole pairs reach the external read-out, η_c is, therefore, defined as the collection efficiency and is determined by the electric field distribution within the device and by the interplay between the different recombination mechanism.

The external quantum efficiency can thus be redefined as:

$$\eta_{ex} = (1 - R)\, \eta_q\, \eta_c \tag{1.6}$$

and related the responsivity with the following expression:

$$Resp = \frac{q\, \eta_{ex}\, \lambda}{h\, c} \tag{1.7}$$

Two other important parameters to evaluate the performances of a photodetector are the noise-equivalent-power (NEP) and the detectivity of the device. The NEP represents the minimum optical power that can be detected by the device and, assuming that the shot noise associated with dark current is the dominating noise mechanism, can be expressed:

$$\mathrm{NEP} = \frac{(2\, e\, I_d)^{1/2}}{Resp} \tag{1.8}$$

with I_d the dark current. The detectivity is defined as $D = \mathrm{NEP}^{-1}$. To make the latter an absolute parameter that allows to compare the performance of two devices, it is better to normalize it for the square root of the active area A of the device. The specific detectivity will be:

$$D^* = \frac{(A)^{1/2}}{\mathrm{NEP}} \tag{1.9}$$

1.2 Avalanche photodiode

In this section we analyze a type of photodetector that have the possibility to work as an avalanche photodiode (APD) [7,8]. These devices feature and internal gain at high reverse bias, i.e. electric fields in the depletion zone $> 10^5$ V/cm.

The primary physical mechanism of the APDs is schematized in Fig 1.4. In the presence of a high electric field in the depletion region, the electrons generated as a result of the absorption of photons, will acquire a high kinetic energy. This energy will be sufficient to promote, by means of collisions, the electrons from the valance band to the conduction one and therefore to generate new electron-hole pairs. The latter will also gain kinetic energy that will result in the promotion of another electron-hole pair, thus generating a chain reaction with a consequent avalanche that will lead, for a specific high value of reverse bias, to the breakdown of the junction.

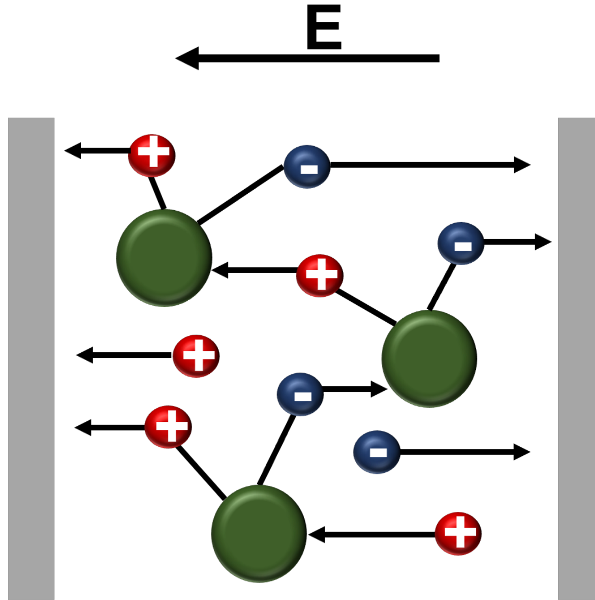

Figure 1.4: Basic principle of the avalanche generated from the electrons and holes with kinetic energy higher that the ionization energy of the semiconductor.

The required impact-ionization energy is $\geq 3/2Eg$. The electrons and holes in the semiconductor can have different ionization coefficients, alpha and beta respectively defined as:

$$\alpha, \beta = a_{\alpha/\beta}\, exp\left(\frac{-b_{\alpha/\beta}}{E}\right) \tag{1.10}$$

where $a_{\alpha/\beta}$ and $b_{\alpha/\beta}$ depend on the material itself, and E is the electric field. It is thus possible to define a ratio of these coefficients $k = \beta/\alpha$ which will be one of the elements to be analyzed in order to choose the optimal semiconductor to use as APD.

A key feature of the avalanche photodiode, that defines its performance, is the response time. The latter is mainly influenced by three factors. The first is τ_{diff}, the time taken by the electron and the hole generated outside the depletion zone to reach it. The second is τ_{tr}, the transit time of the charges in the depletion zone. The third is τ_{av}, the avalanche build-up time. Indeed, an $e - h$ pair does not instantly generate the avalanche, but it will take a time (τ_{av}) to reach a constant value of the multiplication factor M for a fixed bias. The two time constants longest of this three time constants will set the response time of the device. The τ_{diff} and τ_{tr} depend mainly on the thickness d of the intrinsic zone. For this reason, a reduction of the latter would lead to a reduction of these two with an improvement in the response speed of the device. At the same time, however, a reduction of d would increase the capacity of the junction and a reduction of the active zone for the absorption of photons. For these reasons it is necessary to find a compromise between the advantages and disadvantages related to the reduction of the thickness of the depletion zone. The avalanche build-up time τ_{av} can be defined as:

$$\tau_{av} = M\,\tau \tag{1.11}$$

where M is the multiplication factor and τ is the transit time in the avalanche region between two ionization events. It should be noted the difference between τ and τ_{tr}. The first is the transit time between two ionization events, the second is the absolute transit time in the depletion region. The average time between two ionization events τ strongly depends on the ratio of the ionization coefficients k. In fact, semiconductors with very different ionization coefficients for electrons and holes will feature a small τ and therefore a small τ_{av} [9]. On the contrary, if the ionization coefficients do not differ much it will take a longer time to reach a constant M (higher τ_{av}). Silicon falls in the first category featuring a much greater ionization coefficient for electrons α_i as compared to holes β_i, resulting in a short τ_{av} and therefore a good response time of the device. An example of the second case is germanium featuring a ratio between the ionization coefficients $k = 2$ and therefore with respect to an APD in Si there will be a greater build-up time of the avalanche and therefore a lower response time.

Experimentally one can estimate the multiplication factor of an APD as:

$$M(V) = \frac{I_{tot}(V) - I_d(V)}{I_{tot}(V_0) - I_d(V_0)} = \frac{I_{ph}(V)}{I_{ph}(V_0)} \tag{1.12}$$

$I_d(V)$ and $I_{ph}(V)$ are the dark current and the photocurrent as a function of the voltage V, and $I_{tot}(V)$ their sum, while $I_d(V_0)$ and $I_{ph}(V_0)$ are the dark current and the photocurrent at a selected reference voltage V_0, and $I_{tot}(V_0)$ their sum. Fig 1.5 shows $I_d(V)$ and $I_{tot}(V)$ for the case of a silicon APD (panel a) and the resulting value of M obtained using $V_0 = 3$V as a reference bias.

When the applied voltage is equal to the breakdown voltage (V_{BD}) there will be a very rapid growth of the dark current which will become predominant. Knowing the energy gap E_g of the material and the dopant concentration N in the intrinsic region, it is possible to estimate V_{BD} [10]:

$$V_{BD} = 60 \frac{E_g}{1.1}^{3/2} \frac{N}{10^{16}}^{3/4} \tag{1.13}$$

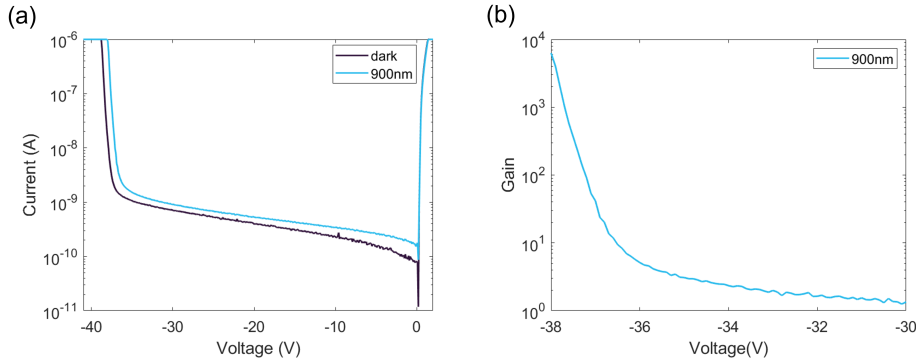

Figure 1.5: (a) IV curve under dark condition (dark line) and under illumination at 900 nm (blue line); (b) Multiplication factor as a function of the bias at 900 nm.

Furthermore, the Miller formula [11] establishes a semi-empirical relationship between the multiplication factor M and V_{BD}:

$$1-\frac{1}{M}=\left(\frac{V}{V_{BD}}\right)^{n} \tag{1.14}$$

where V is the applied bias and n is typically comprised between 2 and 4 depending on the material under consideration. From this formula it can be observed that for V tending to the breakdown voltage, the multiplication factor will tend to infinity, thus limiting the validity of the formula for estimating M only for low currents or far from the breakdown voltage. Instead for high currents the Miller formula [11] can be written as:

$$1-\frac{1}{M}=\left(\frac{V-(I_{d0}+I_{ph0})MR}{V_{BD}}\right)^{n} \tag{1.15}$$

with I_{d0} and I_{ph0} the dark and photocurrent at the reference voltage, and R the equivalent resistance of the photodiode. By solving this transcendental equation we can obtain the expected theoretical trend of the multiplication factor as a function of V also for voltages close to the breakdown.

The final gain of an avalanche photodiode is also affected by crystal quality. For example, in the case of crystals in which there are defects, the latter can trigger local breakdowns that will induced an early breakdown with consequent reduction of the maximum achievable multiplication factor. For this reason, an optimized epitaxial growth and device fabrication are essential for the development of avalanche photodiodes.

1.3 Single photon avalanche diode

Single Photon Avalanche Diodes (SPADs) are used to detect single photons. Their operating principle is based on applying bias V exceeding the breakdown bias::

$$V = V_{BD} + V_{EX} \tag{1.16}$$

being V_{EX} the volts applied in addition to the breakdown voltage. In this condition, the electron-hole pair generated as a result of the absorption of a

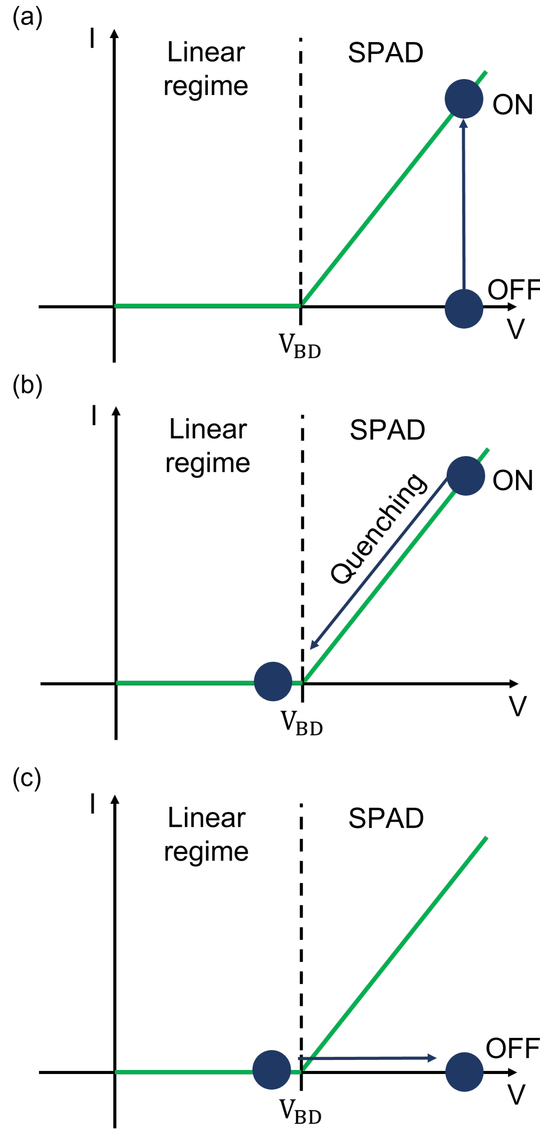

Figure 1.6: The three phases of SPAD operation. (a) the SPAD is set on the ON mode SPAD by applying a bias $V > V_{BD}$; (b) Quenching of the avalanche setting $V < V_{BD}$; (c) Returning to the initial condition;

photon may trigger an avalanche giving rise to a measurable current pulse. This allows the detection of single photons. The avalanche is then damped by a quenching circuit required to bring the SPAD back to its initial condition. Those phases of SPAD operation are shown in Fig 1.6.

Unfortunately, even a single charge generated by the thermal noise can lead to an avalanche generating "dark counts". For this reason, in order to have an efficient SPAD, the thermal generation must be minimized. One solution can be to operate at cryogenic temperatures or alternatively to operate in Gated-mode. In this mode, briefly described in (Fig 1.7), the SPAD will not operate continuously but will have ON-times and OFF-times. In the ON-time the applied voltage $V > V_{BD}$ causes the generation of an avalanche pulse following the detection of the photon. Subsequently, the device is set in an OFF state by applying a voltage $V < V_{BD}$ bringing the SPAD back to the initial condition.

The response of the SPAD to the detection of a single photon will not be instantaneous but will occur with a certain delay called timing jitter, depending on the size of the absorption zone. The recovery time of a SPAD is instead defined as a "dead time" and will be the time following the absorption of a photon in which the device will not be able to detect another one.

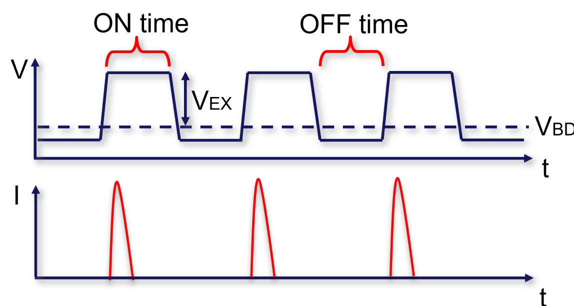

Figure 1.7: Sequence of current pulses (bottom panel) generated for each ON-TIME of the SPAD (top panel).

Another important parameter for defining the performance of a SPAD is the Photon Detection Efficiency (PDE). The latter can be defined as the product between the absorption probability (P_{abs}) and the triggering probability [12] (P_{trig}). The recombination of the generated electron-hole pair can also influence the final PDE, and depends on the density of the defects of the material that can operate as recombination and generation centers.

To overcome the problem of the dead-time of the SPAD there is the possibility to fabricate SPAD arrays. These can be both 1D and 2D and allow during the dead time of the single element of the array to detect the next incident photon using another element of the array in order to obtain a continuous detection. The main problem of a SPAD array is the cross-talk that can take place between two elements of the array that are close to each other. This is due to the fact that when an element of the array is in a state of avalanche some charges will be able to emit photons due to energy relaxation. These photons can be detected by the first neighbours that will trigger another avalanche that will overlap with the original one, increasing in the noise of the measurement.

Chapter 2

3D microcrystals

In this second chapter we analyze the growth of 3D self-assembled microcrystals by Low Energy Plasma Enhanced Chemical Vapour Deposition (LEPECVD). The different morphologies of these microcrystals allow to control their doping profile, their responsivity and their efficiency in the interaction with the incident light. For this reason, after the description of the growth process, the theoretical approaches used for the modelling of crystal morphology and the analysis of their electrical and optical properties, will be presented.

2.1 3D self-assembled microcrystal 21
2.2 LEPECVD growth 22
2.3 Modelling of microcrystal growth 24
2.3.1 Microcrystals defects 28
2.4 Electronic and optical modelling 29
2.4.1 Electronic modelling 29
2.4.2 Optical modelling 30

2.1 3D self-assembled microcrystal

Three-dimensional (3D) microcrystals are obtained starting from a Si substrate[2] patterned by means of electron or optical lithography and deep Reactive Ion Etching (RIE). Fig 2.1 (a,b) shows a Scanning Electron Microscope (SEM) image of a patterned silicon substrate.

Each wafer features several patterns that can have an hexagonal or square arrangement. Furthermore, the Si pillars can have different geometries, differing in the width W of the pillars and the gap G between them. The etch depth is typically around 10 μm, while W and G vary in the 1- 4 μm range (Fig 2.2).

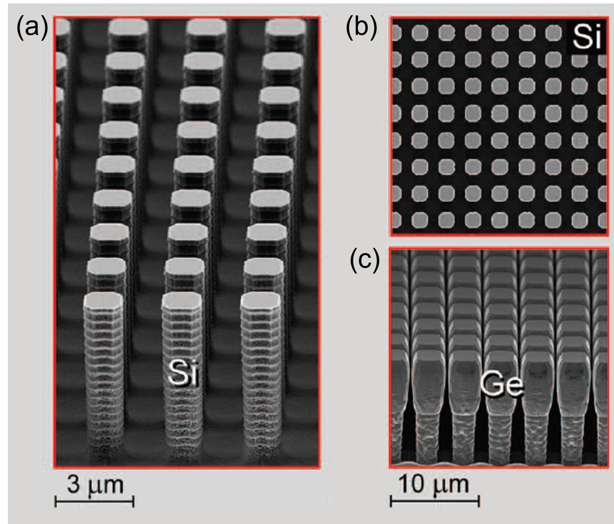

Figure 2.1: Bird's eye view (a) and top-view (b) of patterned Si pillars. (c) 3D Ge microcrystals obtained by LEPECVD. Figure adapted from Ref. 2

2.2 LEPECVD growth

LEPECVD is a variant of thermal Chemical Vapour Deposition [13] (CVD). The latter is based on a vacuum chamber hosting the substrate that is heated by two lamps placed outside a quartz tube (Fig 2.3). Subsequently, the precursors for the growth of Si and Ge are inserted into the chamber, i.e. silane (SiH_4) and germane (GeH_4) respectively. The high temperature of the substrate activates the chemical decomposition reactions of the precursors thus allowing the deposition of Si and Ge adatoms. In a CVD the growth rate strongly depends on the activation temperature of the process. This makes the control of composition and morphology of the epilayer rather challenging.

As already mentioned, all the 3D microcrystals analyzed in this thesis were grown with LEPECVD machine.

The LEPECVD is a variant of CVD, where the precursors are not activated by the temperature of the substrate but by a low-energy high density plasma (ion energy a few eV and ion density around $10^{17}\mathrm{m}^{-3}$).[14,15] This feature provides several advantages over standard CVD. First of all the growth rate does not depend on substrate temperature. Instead it depends on the plasma density and flow of the precursors. In this way it is possible to have both a small growth rate such as 0.4 nm/s for nanometric depositions and a higher growth rate of 5 nm/s for thicker films. Another advantage is that the LEPECVD deposition is an out of equilibrium process and therefore is dominated by kinetics and not thermodynamic phenomena[16]. This is a key-factor in the growth of faceted microcrystals. A sketch of the LEPECVD reactor is shown in Fig 2.4.

The main chamber is held at a pressure of 10^{-8} mbar by means of a turbomolecular pump. The substrate is loaded into the deposition chamber by means of a loadlock so as not to break the vacuum and it is placed in the upper

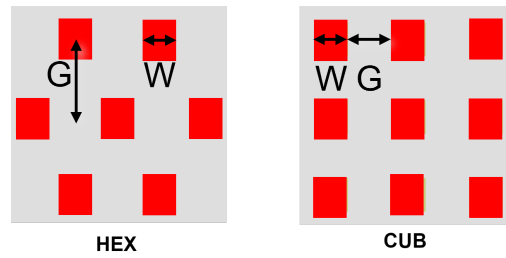

Figure 2.2: Sketch of the Si pillars in the hexagonal (a) and cubic (b) pattern configuration. The patterns can have different gap (G) between the pillars and width (W) of the pillar itself.

part of the chamber with the polished surface facing the lower part where the argon (Ar) plasma is present. Above the substrate there is a heater controlling the temperature, that can be changed to optimize the crystal growth. The argon plasma is generated by the ionization of Ar which take place by means of thermionic emission from a tantalum filament. The plasma is ignited by means of a DC arc discharge from the negatively biased filament to the grounded chamber walls. In this way it is possible to control the plasma energy by means of the voltage applied to the filament and its density by the DC arc current. A grounded anode and a DC magnetic field are used to obtained a dense, uniform plasma close to the substrate.

Finally, the precursor gases are introduced into the main chamber by the gas ring placed under the substrate, bringing the internal pressure of the chamber to 10^{-2} mbar. The precursors used in the growth of homoepitaxial (Si/Si) or heteroepitaxial (Ge/Si) 3D self-assembled microcrystals are: silane (SiH_4), germane (GeH_4), diborane (B_2H_6) for p-doping and phosphine (PH_3) for n-doping.

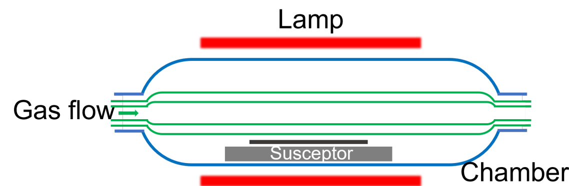

Figure 2.3: Sketch of a CVD chamber. The sample is placed on a susceptor that is heated by the external lamps. The gas of the precursors is flowing into the chamber.

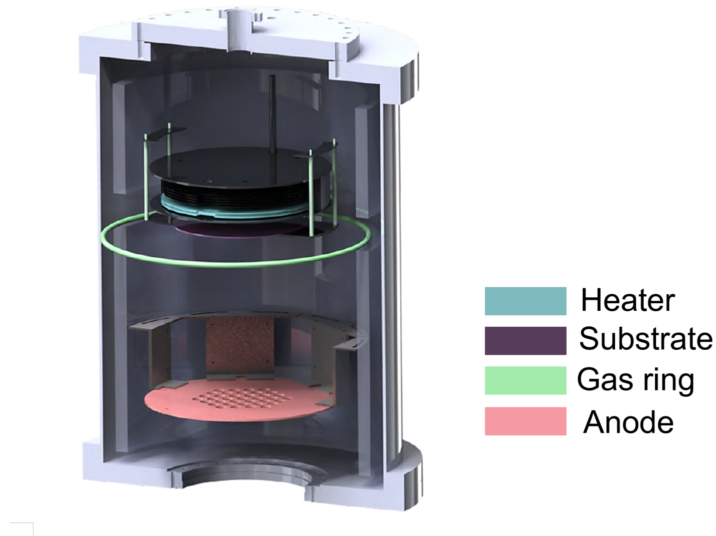

Figure 2.4: Sketch of a LEPECVD reactor with the main elements: heater, substrate, gas ring and anode.

2.3 Modelling of microcrystal growth

As already mentioned, starting from etched Si pillars it is possible, by means of LEPECVD, to obtain 3D self-assembled microcrystals of Si/Si or Ge/Si. During growth on a patterned substrate microcrystals exhibiting low surface energy facets are formed. In thermal CVD this leads to a strong reduction of the growth rate. The microcrystal will then expand laterally due to diffusion effects until merging between adjacent micro crystals takes place[17]. Instead, during LEPECVD the vertical growth of 3D microcrystals, with a self-limited lateral expansion, takes place (Fig 2.1(c), Fig 2.5). This condition is guaranteed by the high growth rates of LEPECVD which ensure that the final morphology of the microcrystal is defined by the kinetics of the different facets and not by thermodynamic phenomena dominating conventional CVD growth. In detail, the final shape will be the one that allows the minimization of the overall growth rate, thus making the slower facets dominant.

As seen in Fig 2.2, the pre-patterned Si substrate can have a cubic or hexagonal configuration, and can be characterized by different G and W parameters. Due to these different initial conditions it is possible to obtain, after the deposition with LEPECVD of Si or Ge, patterns consisting of microcrystals with different morphologies. The names of the patterns that we will analyze in the following chapters and their geometric characteristics, Width (W) and Gap (G) are reported in Fig 2.6. The top of these microcrystals is characterized by the presence of [001],[111] and [113] facets. Each pattern consists of microcrystals with different "weights" of these facets, thus it is possible to obtain microcrystals with a more or less inclined top surface. For this reason we have decided to classify these patterns into two categories. The microcrystals dominated by [111] and [113] facets will be indicated as predominantly faceted, while those

dominated by the [001] surface will be indicated as predominantly flat. This distinction is based on the degree of faceting of the microcrystal, calculated as:

$$D_{fac} = \frac{S_{tot} - S_{001}}{S_{tot}} \tag{2.1}$$

S_{001} is the area of the [001] facet, while S_{tot} is the projected area of the top surface of the microcrystal on the plane normal to the [001] direction.

Fig 2.7 shows the patterns, divided into the two categories based on the degree of faceting. We call predominantly faceted the patterns with a degree of faceting greater than 90%, while the others are predominantly flat.

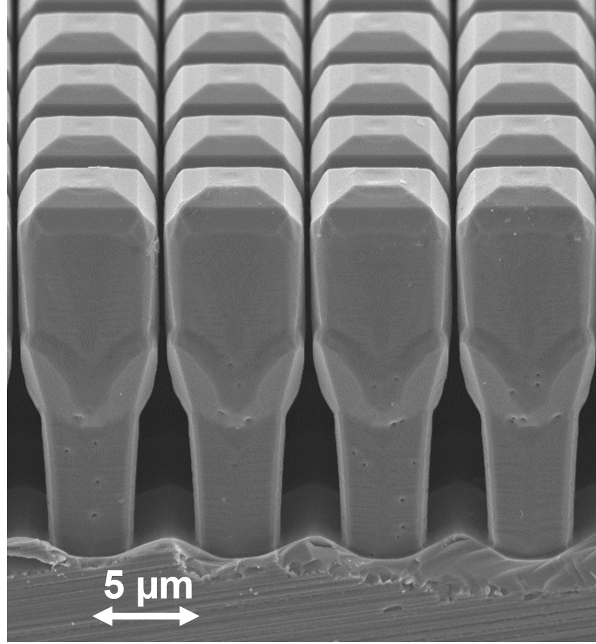

Figure 2.5: SEM image of a pattern of 3D self-assembled Si microcrystals with limited lateral expansion.

(a)

Pattern	W (µm)	G (µm)	CONF.
A	2	2	cub
C	2	4	cub
G	2	3	cub
O	4	3	cub

(b)

Pattern	W (µm)	G (µm)	CONF.
K	2	4	hex
N	3	4	cub

Figure 2.6: Table of the patterns used for device fabrication in this thesis, defining the Width of the Si pillar (W), the Gap between them (G) and the configuration. (a) Geometric characteristic of Ge/Si microcrystals, and (b) of Si microcrystals.

The growth of microcrystals on patterned substrates can be modelled using the Borgstrom construction (Fig 2.8(a,b)) [3]. Starting from the different speeds

of the facets in the different directions $v(\boldsymbol{n})$ it is possible to define growth fronts for each of them. Considering the intersection of each growth front with its first neighbours, it is possible to make the convolution and obtain the shape of the microcrystal at each instant during growth.

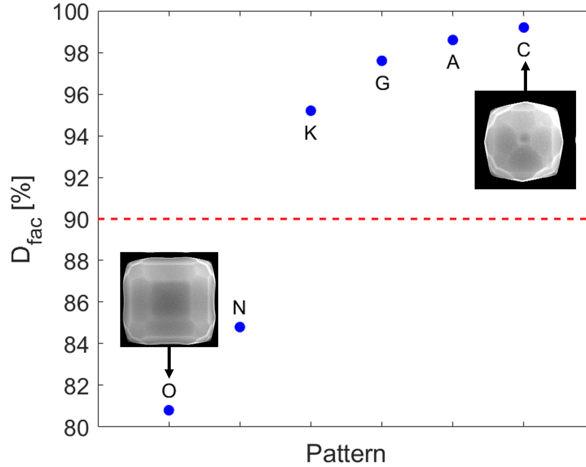

Figure 2.7: Representation of the degree of faceting (blue circle) of the six different patterns that will be analyzed in this thesis. The red line represents the boundary between the classification of patterns as predominantly faceted (above 90%) and predominantly flat (below 90%).

Specifically, to predict the morphology of the 3D self-assembled microcrystals, grown in the LEPECVD, it is necessary to develop simulations that take into account all the processes determining $v(\boldsymbol{n})$. These simulations have been performed by Prof. R. Bergamaschini (University of Milano-Bicocca). In such 2D simulations, the temporal evolution during the growth of each facet is analyzed. To do this, the growth front is divided in a set of mesh points (Fig 2.9(a)). For each point a rate equation must be solved to obtain the density of adatoms at the growth-front [3]:

$$\frac{dN}{dt} = \Phi - \frac{N}{\tau_d} + D\frac{\partial^2 N}{\partial s^2} - \frac{N}{\tau_c} \tag{2.2}$$

where Φ is the flux of incident atoms, τ_d the desorption time, D the adatom diffusivity and τ_c the crystallization time. In this equation the first term takes into account the flux of incident atoms that actually depends on the facet orientation and the shielding by the microcrystals near-neighbors. Considering these effects, each point of the facet can only be reached from a limited number of directions (Fig 2.8(c,d)) [3].

The second term takes into account the atom desorption in the gas phase, while the third considers surface diffusion of the atoms. This effect will be strongly depend on the deposition temperature. The fourth and final term represents the incorporation of the adatoms into the crystal. This effect takes place by clustering or incorporation into steps. In Fig 2.9(b) it can be seen how

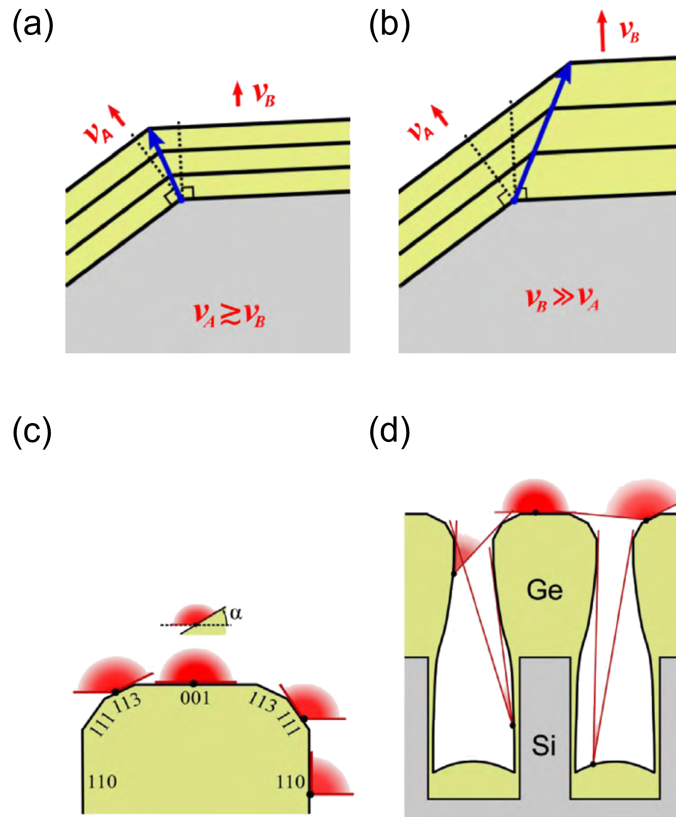

Figure 2.8: In the top panels sketch representing the two possible case of a Borgstrom construction are represented. In the panel (a) the facet B has a growth velocity almost equal to the facet A, resulting in facets of similar size. Instead, in the panel (b) the growth rate of facet B is much greater than that of facet A, resulting in a reduction of the size of facet B. In the bottom panels are represented the dependence of the incident flux on the facet inclination (c), and on the shielding effect (d). Figure presented with the permission of [3].

the growth profile of a microcrystal observed by the SEM image of the cross-section perfectly overlaps the simulated profile obtained by solving the system of rate equations for each point of the mesh.

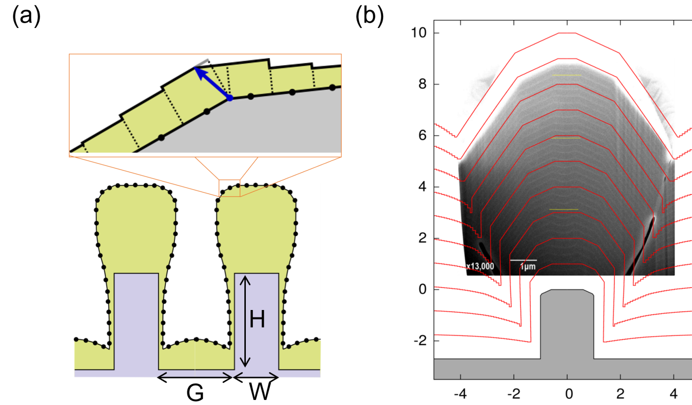

Figure 2.9: (a) Meshing of the growth profile of the microcrystal; (b) Simulated growth profile (red continuous line) overlapping a SEM cross-section of the microcrystal. In this case SiGe markers have been periodically embedded during growth to highlight the growth front evolution.

2.3.1 Microcrystals defects

The faceted morphology of a microcrystal influences the evolution of defects in this structure. Transmission Electron Microscopy (TEM) measurements of microcrystal lamellae have been carried out by the group of Prof. K. Volz at the University of Marburg. In the case of homoepitaxial microcrystals, Si/Si, from the TEM images (Fig 2.10) it can be seen that at the interface between the lateral rough surface of the Si pillar and the grown Si many defects are nucleated. These defects continue towards the lateral part of the microcrystal until they are expelled at the surface.

On the contrary, it can be noted that at the interface between the upper part of the Si pillar and the grown microcrystal there is no nucleation of defects that continue up to the top of the microcrystal. This TEM analysis has also been performed for heteroepitaxial microcrystals, Ge/Si [2]. Due to the high lattice mismatch between Ge and Si, 4.2%, misfit dislocations are generated at the interface. This leads, in a standard epilayer, to a high density of dislocations threading trough the Ge epilayer and reaching the film surface. However, as can be observed from the TEM analysis of a lamella of the Ge/Si microcrystal (Fig 2.11), the microcrystals thanks to the faceted morphology have a large percentage of threading dislocations that are expelled at the sidewalls. This effect results in a strong reduction of defects present in the Ge/Si microcrystal compared to an equivalent epilayer. By combining substrate patterning and LEPECVD it is possible to grow 3D self-assembled microcrystals of Si or Ge that can operate as micrometer thick absorbing layer.

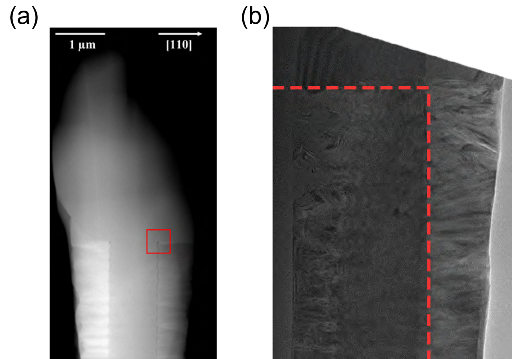

Figure 2.10: TEM analysis of a Si microcrystal: (a) SEM cross-section of the Si lamella; (b) Bright-field TEM of a Si microcrystal.

2.4 Electronic and optical modelling

To exploit Si/Si and Ge/Si microcrystals for photodetection applications, a careful design of the doping profile and therefore of the distribution of the electric field inside the microcrystal is necessary. To this purpose, 2D electronic simulations were carried out by the group of Prof. A. Tosi at the Politecnico di Milano using the Centaurus TCAD software.

In addition to the analysis of the electronic properties, we have also analyzed the optical properties of these structures. To simulate the latter we implement 2D Finite Difference Time Domain (FDTD) simulations using the Lumerical software.

2.4.1 Electronic modelling

Electronic simulations are performed for different doping profiles based on the possible photodetection applications of the microcrystals. Since the Ge microcrystals will be used as NIR photodetectors from 1200 to 1800 nm, the first family of simulations is made for a simple *p*-*i*-*n* junction. The top p^+ contact has a doping of $8 \times 10^{18}\text{cm}^{-3}$ and a thickness of 200 nm. The intrinsic zone is lightly p-doped ($1 \times 10^{16}\text{cm}^{-3}$), with a thickness of 5μm (Fig 2.12 (a)).

On the other hand, a microcrystal of Ge that operates as APD has not been simulated and grown due to the challenges of the use of germanium as a multiplication material (see section 1.2).

The second family of simulations have been carried out for Si microcrystals. In this case, we did not want to investigate a standard *p*-*i*-*n* doping profile but a more complex profile that allows their application as APD or SPAD. An example of such doping profile is shown in Fig 2.12 (b). Two regions can be identified: an absorption region and a multiplication region, which will require an electric field of approximately 10^5 V/cm.

The results obtained from these simulations allowed us to define the correct doping profiles to be grown (doping concentration and thickness) to optimize the

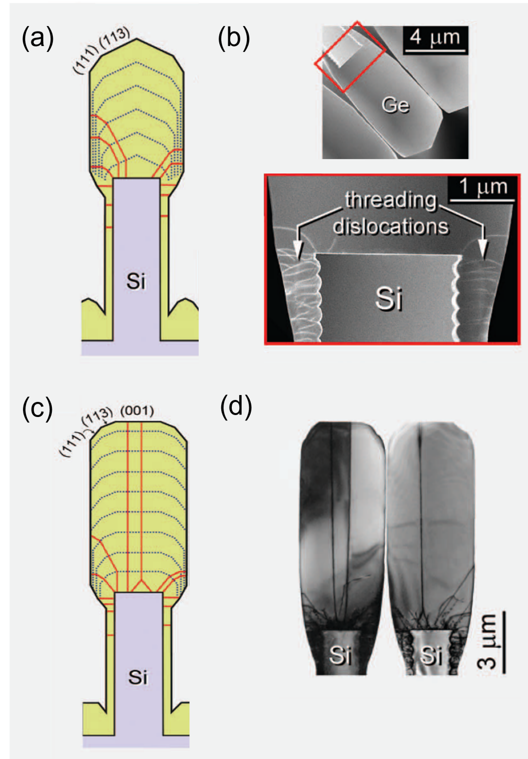

Figure 2.11: TEM analysis of Ge microcrystals: (a) Sketch of a faceted microcrystal, with dislocations bending towards the lateral surfaces. (b) Bright-field TEM image of faceted microcrystal with dislocations that go towards the sidewalls. (c) Sketch of a non-faceted microcrystal, with straight dislocations reaching the top surface. (d) TEM image of a non-faceted microcrystal with a small density of dislocation that go also towards the top of the microcrystal. Figure adapted from Ref. 2.

distribution of the electric field, and in the case of APD also the avalanche probability, inside the microcrystal. A typical output of the electronic simulations of a Si microcrystal is shown in Fig 2.13.

2.4.2 Optical modelling

We have already seen in 2.3.1 how the faceted morphology of the microcrystals can influence the density of defects, allowing the growth of micrometer thick absorbing layers. The microcrystals, due to their particular morphology and specifically their inclined top facets, will activate light trapping effects. For this reason I have carried out simulations to test this property of the microcrystals. In detail, I have performed FDTD simulations using the Lumerical software to solve Maxwell's equations in 2D for different microcrystals patterns.

A sketch of the building blocks of the simulation is represented in Fig 2.14. The different elements to be defined in the software are:

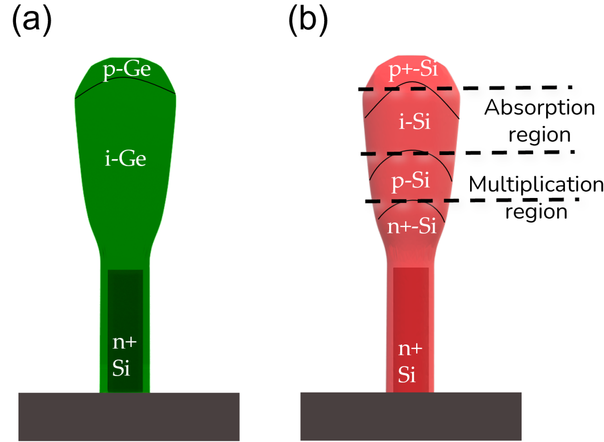

Figure 2.12: (a) Doping profile of a *p-i-n* Ge microcrystal operating as photodetector; (b) Doping profile of a Si microcrystal operating as APD or SPAD.

1. the morphology of the microcrystal to be analyzed, implemented starting from SEM cross-section images.
2. the refractive index of the semiconductor, real and imaginary part, for the wavelength range of interest for the simulation.
3. the type of source of the incoming light, which in our case is a plane wave that illuminates the microcrystal from the top.
4. FDTD domain of simulation, tailored on the geometry of the pattern under investigation;
5. Boundary conditions to be imposed in the two dimensions of the simulation. Specifically, they are Bloch boundary conditions in the horizontal X-direction to consider the periodicity of the pattern at least in one direction, and Perfectly Matched Layers (PML) in the Y-direction. The latter works as an artificial absorbing layer, forcing the field to zero by absorbing the light with low reflectance.
6. Frequency-domain field monitors to acquire the field profile in the frequency domain. A first one is placed between the source and the top facet of the microcrystal and allows to calculate the light entering the microcrystal equal to $1 - R$ (with R = fraction of reflected light), and a second one at the output of the microcrystal that calculates the transmitted light T (T = fraction of transmitted power).

By setting all these parameters from the simulation it is possible to calculate the fraction of power absorbed by the microcrystal as:

$$A = 1 - R - T \tag{2.3}$$

The latter allow us to define the absorption properties of the microcrystals as a function of the morphology and the incident wavelength.

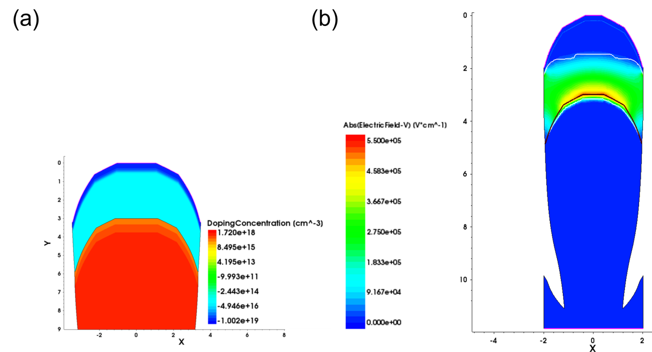

Figure 2.13: Electronic simulation: (a) An example of simulated doping profile inside a Si microcrystal; (b) Simulated electric field distribution linked to the doping profile concentration shown in (a).

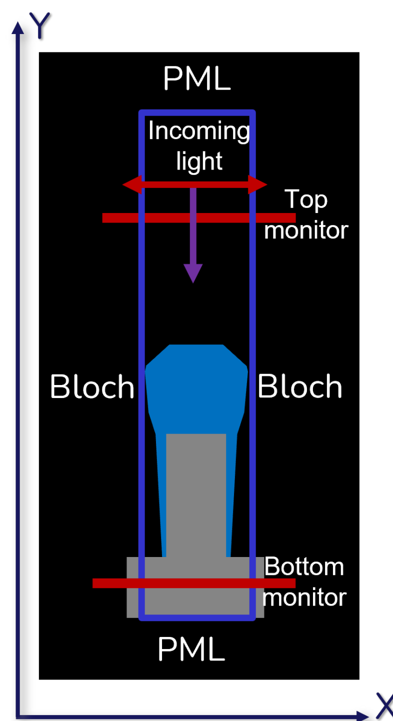

Figure 2.14: Sketch of the microcrystal structure inside the Lumerical software. The setted parameters of the FDTD simulation are present in the figure.

Chapter 3

Ge/Si microcrystals

In this third chapter the electro-optical properties of Ge/Si microcrystals are investigated. The analysis starts from the optical simulation (3.1.1) to test the optical properties of a Ge/Si microcrystal and continues with the electro-optical characterization of single microcrystals (3.1.2). Then, a fabrication process that allows to use an array of Ge/Si microcrystals as a photodetector is presented (3.2.1). Eventually, the electro-optical characterization of this device is reported (3.2.2).

3.1 Photodetection with Ge/Si self-assembled microcrystal 33
3.1.1 FDTD modelling of Ge/Si microcrystals 34
3.1.2 Electro-optical characterization of a single Ge/Si microcrystal 37
3.2 Photodetectors based on Ge/Si microcrystal arrays 40
3.2.1 Fabrication process 40
3.2.2 Electro-optical characterization of the device 43

3.1 Photodetection with Ge/Si self-assembled microcrystal

Arrays of Ge/Si microcrystals have been grown by LEPECVD, with a *p-i-n* doping profile (see Fig 2.12 (a)). Starting from a n^{++} patterned silicon substrate, 5μm of intrinsic Ge (p-type background 1×10^{16}cm^{-3}), and a top contact of 200 nm of p^{+}Ge (8×10^{18}cm^{-3}) are grown. In this way we obtain a photodetector with an intrinsic internal electric field linked to the built-in potential of the *p-i-n* junction. Several patterns, with different geometries but identical thickness and doping profile, have been analyzed. The most significant are patterns A,C and O (Fig 2.6), whose SEM images (top- and side-view) are shown in Fig 3.1. These patterns feature different morphologies, more or less faceted, and different periodicity.

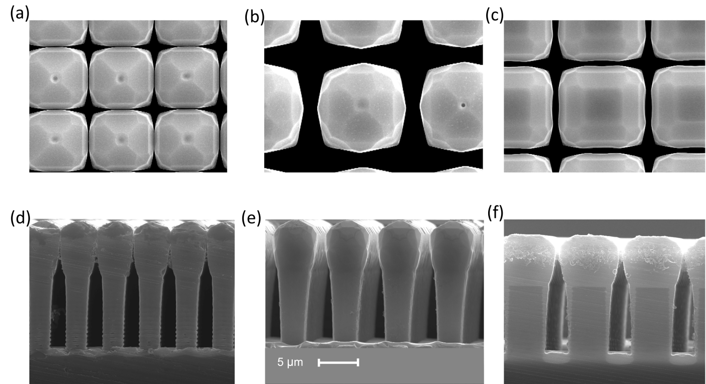

Figure 3.1: SEM images of three different patterns: (a)(b)(c) top-view of patterns A, C and O; (d)(e)(f) side-view of patterns A,C and O. Figure presented with the permission of [5]

3.1.1 FDTD modelling of Ge/Si microcrystals

After the growth of the Ge/Si microcrystals the analysis of their optical properties by means of FDTD simulation has been performed. The building blocks of the simulation are those reported in the previous chapter (see Fig 2.14). In particular, starting from the SEM image of the cross-section of the microcrystals (see Fig 3.1), the morphology of the microcrystals has been reconstructed by means of truncated pyramids within the Lumerical software. The boundary conditions, the source and the monitors chosen are those that have been defined in section 2.4.2.

To better understand the role played by faceting and periodicity, the optical properties of the microcrystals array have been compared with those of a reference planar epilayer, featuring the same Ge thickness. For this reason the simulations have been carried out for both structures and the sketches of the two simulation domains are represented in Fig 3.2.

From the input and output field monitor of these simulations it is possible to calculate the fraction of absorbed power for the patterns A, C, O and for the Ge epilayer. The results are shown in Fig 3.3. The fraction of absorbed power for the three patterns is greater than that of the epilayer, and the predominantly faceted microcrystals (A and C) absorb the incident light more efficiently than the predominantly flat one (O). Furthermore pattern C, which has the highest degree of faceting (see Fig 2.7), absorbs more power even compared to the other predominantly faceted patterns. If we compare the fraction of power absorbed by pattern C and by the Ge epilayer, and calculate the ratio between these two quantities (Fig 3.4), it can be seen that this ratio is always greater than one. Moreover the enhancement of the fraction of absorbed power of the pattern with respect to the epilayer, is particularly strong in the indirect regime of absorption of Ge (1550-1800 nm). This trend is observed also for the other two patterns A and O (see Appendix A.1).

The enhanced microcrystal absorption, specially at wavelengths in which Ge has a lower absorption coefficient, is related to light trapping effects. As

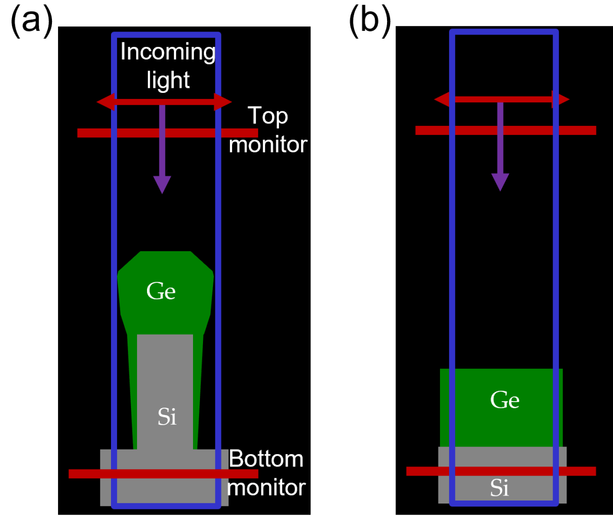

Figure 3.2: (a) Sketch of a single microcrystal simulation domain. The morphology has been obtained from the SEM cross-section image of pattern O; (b) Sketch of the simulation domain for a 5μm thick Ge epilayer.

already mentioned, under vertical illumination, the faceted morphology of the microcrystal generates this light trapping effect with a consequent increase of the optical path within its volume. This condition will allow an increase of the absorbed power in particular at wavelengths longer than 1550 nm. Another kind of light trapping phenomenon take places in the gap between a microcrystal and its closest neighbours. Indeed, the confinement of light in the gap between two microcrystals increases the number of photons entering the Ge absorbing layer, from the side of the microcrystal.

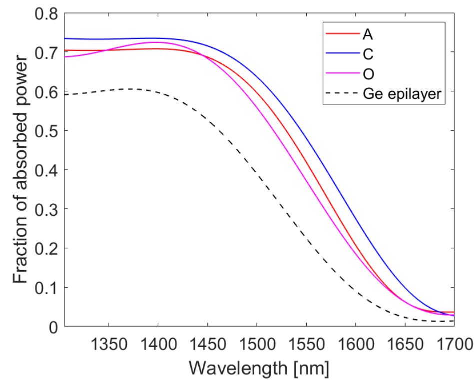

Figure 3.3: Fraction of absorbed power for the three simulated patterns A, C, O and for the 5μm Ge epilayer.

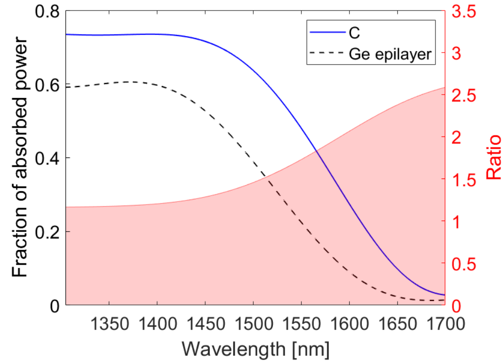

Figure 3.4: The blue continuous line is the fraction of absorbed power for the pattern C, while the black dashed line is the fraction of absorbed power for the Ge planar epilayer. The ratio between these two quantities is represented by the red curve.

To evaluate the effective weight of these two contributions new simulations have been performed for the predominantly faceted microcrystal C and for the predominantly flat microcrystal O by varying the periodicity of the array. The result of these simulations is shown in Fig 3.5.

It can be observed that for pattern C, predominantly faceted, as the periodicity of the array changes, there is no variation in the fraction of absorbed power. For pattern O, predominantly flat, there is a small variation of absorbed power as the distance between a microcrystal and its closest neighbours varies. We can therefore conclude that for the predominantly faceted microcrystals the light trapping will occur mainly within the volume of the microcrystal. For the predominantly flat microcrystals the contribution of the light trapping in the gap between one microcrystal and the other gives a small contribution to the fraction of the absorbed power.

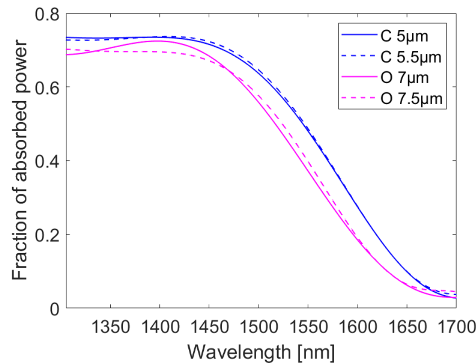

Figure 3.5: Effect of the pattern periodicity on the microcrystal absorption properties. For pattern C a variation of the periodicity of 0.5 μm does not lead to significant changes in the calculated fraction of absorbed power, a small variation is observed in the case of pattern O.

To test whether this optical property can improve the responsivity of a microcrystal based photodetector we proceeded with the electro-optical characterization of a single microcrystal.

3.1.2 Electro-optical characterization of a single Ge/Si microcrystal

An experimental setup has been developed to test the electro-optical properties of a single Ge/Si microcrystal. The main elements of this setup are shown in Fig 3.6(a):

1. Laser source: supercontinuum laser from NKT Photonics with a half-width at half maximum of 10 meV.
2. Confocal microscope: an objective 60× focuses the laser beam on a single microcrystal, with a final spot area of almost 7 μm.
3. Nanomanipulator: equipped with a tip with a diameter of 100 nm, and capable of contacting the top facet of a single microcrystal (Fig 3.6(b,c)).

Using the tip as a top contact and the back surface of the sample as the back one, it is possible to collect the dark current and photocurrent signals.

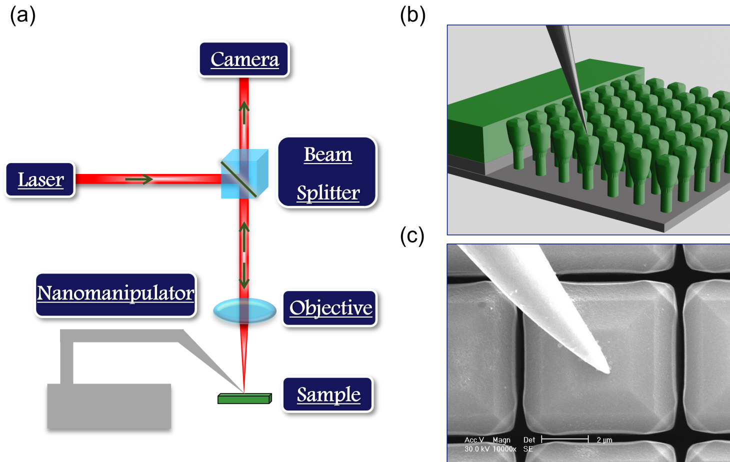

Figure 3.6: (a) Experimental setup based on: a confocal microscope, composed by a beam splitter, a focusing objective, a camera, a supercontinuum laser source and a nanomanipulator; (b) Sketch of the tip landed on the top of a single microcrystal; (c) SEM image of the tip on the microcrystal.

This electro-optical characterization has been carried out for several microcrystals belonging to both the predominantly flat and the predominantly faceted categories. The IV curve obtained, for example, for pattern G, a predominantly faceted microcrystal (see Fig 2.7), is represented in Fig 3.7 (dark line). The expected rectifying behaviour related to the *p-i-n* junction is observed. However, it can be observed that there is a high dark current (50 times higher with respect to the typical Ge-on-Si diodes dark current density of ≈ 10 mA/cm^2 [18]). According to previous literature reports on similar samples [19] a post-growth wet

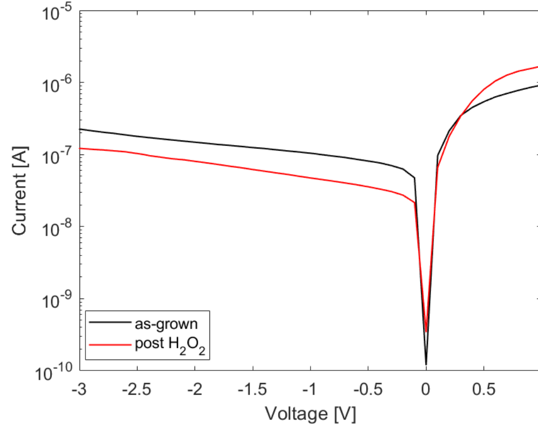

Figure 3.7: Comparison between the IV curve of an as-grown and etched microcrystal from pattern G. We notice that the etching procedure leads to a reduction of the dark-current by ≈ 2.

etching step has been performed to reduce the dark current and improve the rectifying behaviour of *p-i-n* microcrystals. An improvement of the post growth IV curve has been achieved after two minutes H_2O_2 wet etch. The chemical reactions underlying this Ge wet etch are:

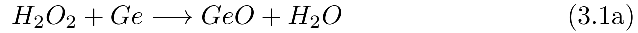

$$H_2O_2 + Ge \longrightarrow GeO + H_2O \tag{3.1a}$$

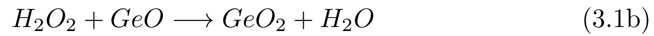

$$H_2O_2 + GeO \longrightarrow GeO_2 + H_2O \tag{3.1b}$$

$$GeO_2(s) \longrightarrow GeO_2(aq) \tag{3.1c}$$

The resulting reduction of the dark current (Fig 3.7(red line)) can be ascribed to the removal of the defected material growing on the Si pillar sidewalls and of the *p*-doped layer formed on the microcrystal sidewalls. As will be better clarified in the next chapter, dopant diffusion on the sidewalls give rise to electric-field hotspots favouring tunnelling and trap-assisted tunnelling effects.

The responsivity of a single Ge microcrystal, is defined as $Resp = I_{ph}/P$. The photocurrent I_{ph} is measured as the difference between the illuminated and dark IV curves without the need of any modulation technique.

The responsivities of a predominantly faceted G microcrystal, and that of an equivalent Ge epilayer photodetector [20], are compared in Fig 3.9(a). It is evident the extension of the microcrystal responsivity in the region of indirect Ge absorption compared to the reference photodetector. This property makes the microcrystals interesting building blocks for the fabrication of Ge photodetectors when a greater sensitivity is required for the 1550-1800 nm wavelength range.

To analyze the dependence of the microcrystal responsivity on its morphology, the responsivity of the G microcrystal (predominantly faceted) has been compared with that of the O (predominantly flat) microcrystal. The comparison between the two normalized responsivities, obtained for a bias of -3V, is shown in Fig 3.8. It can be seen that the more faceted microcrystal G has a greater responsivity in the indirect regime of absorption of germanium, over

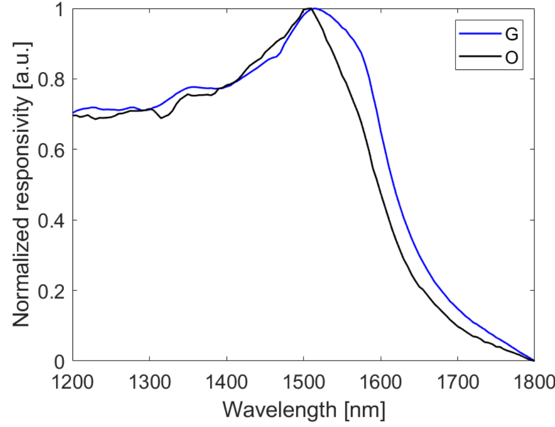

Figure 3.8: Normalized responsivity of a single microcrystal from pattern G (blue line), predominantly faceted, and pattern O, predominantly flat (black line).

1550 nm. This trend is in agreement with the results of the FDTD simulations (see Fig 3.3). The predominantly faceted microcrystals therefore have a higher responsivity originating from a greater fraction of absorbed power (see Appendix A.2).

The photocurrent has been measured for different reverse bias going from -1V to -3V (Fig 3.9(b)). At -1V the responsivity of the single microcrystal is an order of magnitude lower than typical literature values of a *p-i-n* Ge-on-Si photodiode[18]. However, the microcrystal responsivity increases going from -1V to -3V and, at high reverse bias reaches values to those obtained in conventional Ge-on-Si photodiodes (see Ref. 18). This behaviour can be traced back to the comparatively long absorption region of micro-crsytal-based photodetectors which requires a larger reverse bias to efficiently collect the photogenerated carriers.

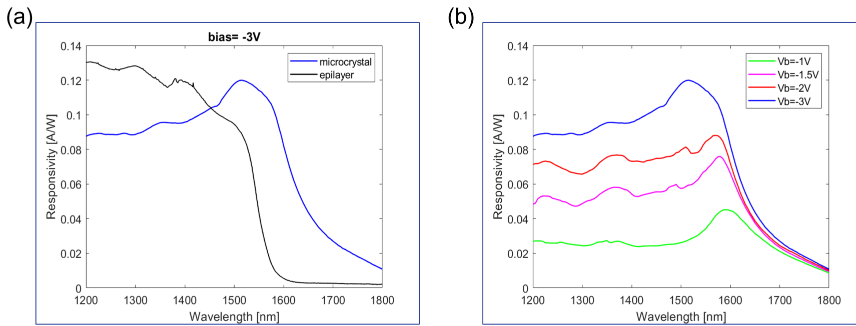

Figure 3.9: (a) Comparison of the responsivity at -3V of a single microcrystal (blue line) and a Ge mesa diode (black line); (b) Responsivity of a single Ge microcrystal from pattern G at -1V (green line), -1.5V (pink line), -2V (red line) and -3V (blue line).

The H_2O_2 wet etch will lead also to a reduction of the final NEP of the

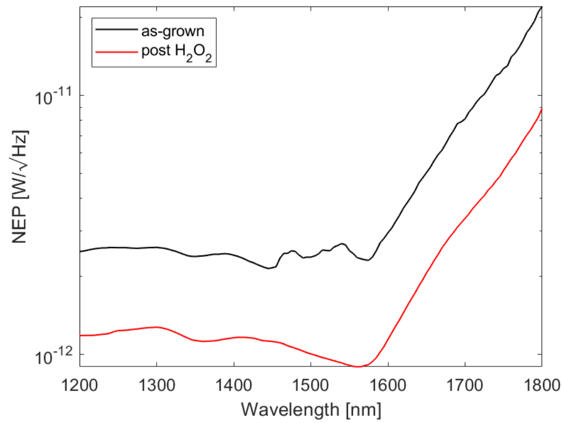

Figure 3.10: NEP of a single microcrystal of pattern G: after growth (black line) and after the H_2O_2 wet etch (red line).

microcrystal, calculated by the formula (1.8) (Fig 3.10).

3.2 Photodetectors based on Ge/Si microcrystal arrays

Once the photoelectric properties of the single microcrystal have been tested, we have developed a photodetector based on microcrystals array. The latter has been fabricated (3.2.1) and characterized (3.2.2).

3.2.1 Fabrication process

The main challenges for the fabrication process of this structure are, the 3D morphology of the microcrystals and the 100-200 nm gap separating the microcrystals. For this reason, a material that can adapt to the 3D morphology and that can bridge the gap between microcrystals must be used as top contact. Obviously, such a material must be transparent to allow vertical illumination.

A possible choice is graphene, that is flexible and almost transparent with an absorption of the incoming light of only 2.4% [21,22].

The steps of the fabrication process are represented in Fig 3.11. The first step is the PECVD deposition of 200 nm of SiO_2 both on the patterned and unpatterned region (Fig 3.11(a)).

Then a step of optical lithography is performed. A positive photoresist AZ5214 is spin coated on the sample at a speed of 6000 rpm for 60s with an acceleration of 500 rpm/s. The spin-coated sample is baked at 110 °C for 90 s. The exposure is made by a laser writer such that after the AZ5214 development, the photoresist can be removed from the patterned region, while it remains on the unpatterned region. In this way in the unpatterned region, the SiO_2 remains protected by the photoresist.

Now the sample is ready for BOE wet etch to remove the SiO_2 from the patterned region. A sketch of the device under fabrication at this stage is shown

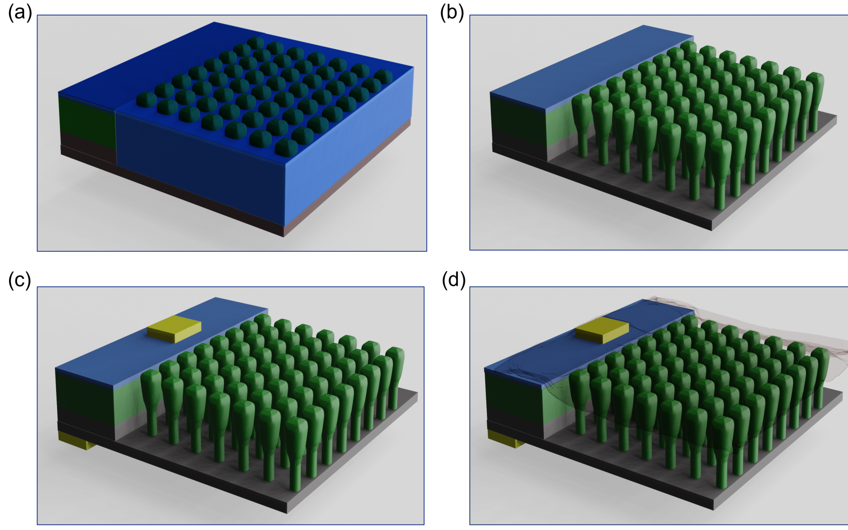

Figure 3.11: (a) Deposition of 200 nm of SiO_2 on all the sample; (b) Removal of SiO_2 just from the patterned region; (c) Evaporation of a Au/Ti metal contact on the unpatterned region; (d) Graphene wet transfer process on the sample.

in Fig 3.11(b).

A second step of optical lithography is necessary to define by evaporation the top metal pad on the unpatterned region (Fig 3.11(c), Fig 3.13(a)). A 200 nm metal layer made of Au/Ti is evaporated. At the end of this process the sample is ready for the last step: the graphene wet transfer process [23] (Fig 3.11(d)). This procedure is performed starting from a commercial graphene layer grown on the two sides of a copper foil (Gr/Cu/Gr). To obtain a graphene single layer it is necessary to perform a Cu etching process. The steps of this process are described here below:

1. A layer of PMMA is spin coated on the Gr/Cu/Gr foil with a velocity of 1000 rpm, reached with an acceleration of 200 rpm/s, for a time of 60 seconds.

2. Bake on a hot plate for 2 minutes at 160°C.

3. Removal of graphene from the lower face of the Cu foil by means of plasma asher. An oxygen plasma is made to react with the carbon of graphene, with a flow of 250 ml/min, at a power of 500 W for one minute. In this way we will have a PMMA/Gr/Cu flake.

4. Wet etching of the Cu by the solutions:

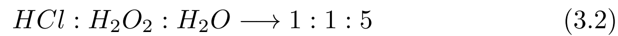

$$HCl : H_2O_2 : H_2O \longrightarrow 1 : 1 : 5 \quad (3.2)$$

for 45 seconds, and then:

$$FeCl_3 : H_2O \longrightarrow 1 : 2 \quad (3.3)$$

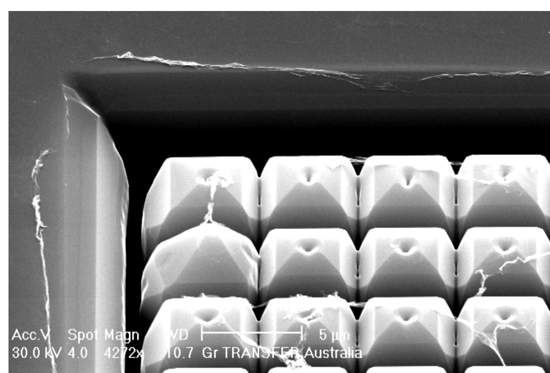

Figure 3.12: SEM image of a single layer of graphene on a microcrystal array after the graphene wet transfer process.

for 4 hours. After each of these wet etching step, the graphene flake is fished with a glass slide and cleaned from contamination particles by placing it in a beaker of deionized water. This ultimately results in a single layer of graphene, with PMMA on it, floating in a water beaker. At the end the PMMA/Gr flake is fished out with the sample, and the remaining water on the sample will be evaporated naturally during the next 10 hours. Subsequently, to optimize adhesion, the sample with graphene is placed on a hot plate at 160°C for 5 minutes.

5. Removal of the PMMA layer on the Gr/sample by means of acetone.

The graphene on the sample obtained from this process is shown in Fig 3.12. The graphene obtained is not continuous and breaks after the removal of the PMMA layer, generating a "spider-web" effect.

The reason for this negative result could be linked to the capillary forces acting during the drying process. These latter are relevant for our pattern of microcrystals featuring a high aspect ratio and a distance between microcrystals of hundreds of nanometers.

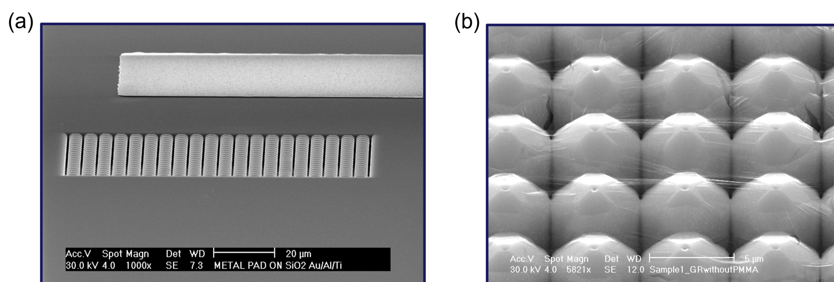

Figure 3.13: (a) Bird's-eye-view of the microcrystal based device prior to graphene transfer. The metal pad deposited on a thick oxide layer and the patterned area are clearly visible; (b) Double graphene layer on the microcrystals array.

To overcome this problem we therefore decided to increase the mechanical strength of the top contact, employing a double layer of graphene. To do this at the end of the first graphene transfer process, the floating PMMA/Gr flake was fished out not using the sample but with another Gr/Cu foil.

At this point, repeating all the graphene transfer steps already described, we obtain a PMMA/Gr/Gr flake which is then fished with the sample. After the removal of PMMA, the result obtained is a double graphene layer on the sample as in Fig 3.13(b). It can be seen how such double-graphene layer is now able to form a continuous top contact.

3.2.2 Electro-optical characterization of the device

Once the fabrication process of the graphene-based device is completed, it is possible to proceed with the characterization of the photoresponse of the microcrystals array. The pattern is top illuminated and the photocurrent is collected at the metal pad, electrically connected to the graphene layer, and at the bottom surface of the sample operating as the back contact. The experimental setup used is based on the supercontinuum laser and the confocal microscope already discussed in 3.1.2. The objective used in this case is 40x with a final spot on the sample of 20 μm and the nanomanipulator is not used since the graphene is operating as top contact. Furthermore, a chopper is inserted between the laser source and the beam splitter operating at 831 Hz. The collected photocurrent signal is amplified by a TransImpedence Amplifier (TIA) and finally demodulated by a Lock-In Amplifier (LIA). The responsivities obtained

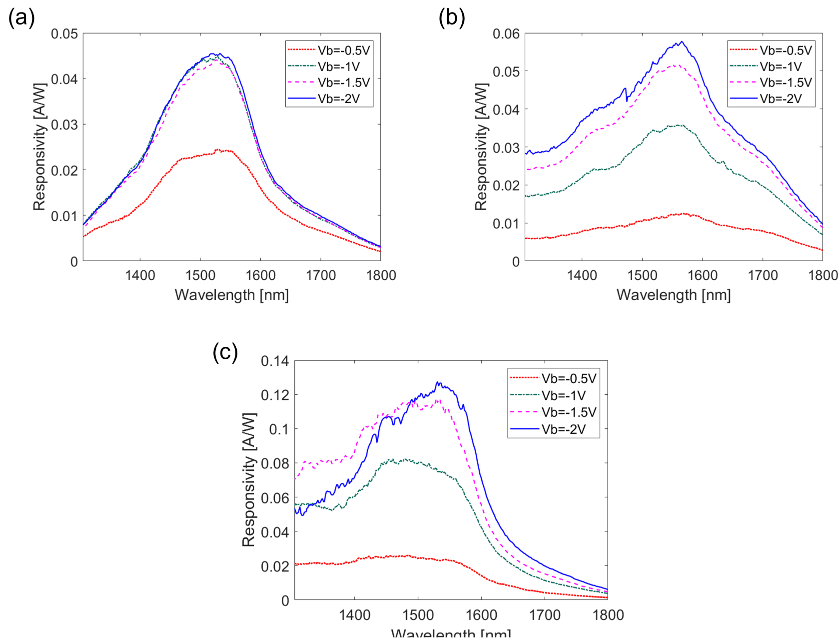

Figure 3.14: Responsivity of the final device of microcrystals array fabricated by the use of graphene as top contact: (a) Pattern A; (b) Pattern C; (c) Pattern O.

for three patterns A, C and O are represented in Fig 3.14(a),(b),(c). Patterns A and C consist of predominantly faceted microcrystals, while pattern O of predominantly flat microcrystals. It can be observed that the responsivities do not drop at 1550 nm, thus confirming the same trend observed for the single Ge microcrystal (Fig 3.9(a)).

In particular, if we compare these three responsivities by normalizing them, it can be observed that the predominantly faceted patterns feature a greater enhancement of the responsivity above 1550 nm. The pattern showing the highest responsivity is the pattern C, i.e. the predominantly faceted pattern with the highest degree of faceting (see Fig 2.7).

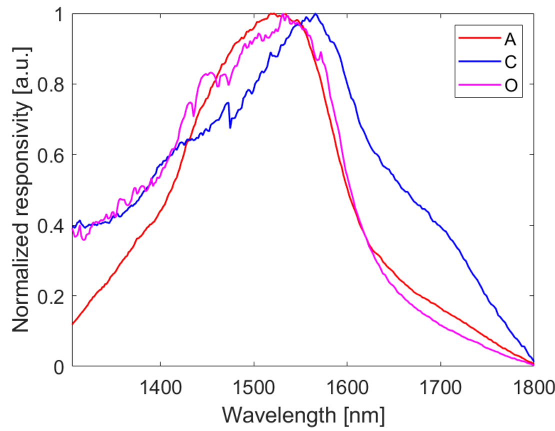

Figure 3.15: Normalized responsivities at -2 V of graphene/Ge microcrystal devices obtained from: Pattern A (red line); Pattern C (blue line); Pattern O (pink line).

A reference, planar, Gr/Ge photodiode has been fabricated in the unpatterned region of the same chip used for the microcrystal based detector (see Fig 3.16(a)). The responsivity measured for the Ge planar device is shown in Fig 3.16(b).

If we compare, for example, the responsivity at -3V for pattern C with that of the Ge planar device we can see how the ratio of these responsivities increases at wavelengths longer than 1550 nm, i.e. in the absorption region of the Ge indirect gap (Fig 3.17). This trend of the ratio between the responsivities confirms the result obtained from FDTD simulations (Fig 3.4). Therefore, the microcrystals show an enhancement of the fraction of absorbed power in the NIR, especially for wavelength greater than 1550 nm, and this effect leads to an enhancement of the responsivity of the microcrystals in this region when compared to an equivalent Ge planar device.

It can be noted that the absolute value of the responsivity of the fabricated device (Fig 3.14) is lower than that of a single microcrystal measured by means of the nanomanipulator (Fig 3.9a). The two photoresponses can be compared in terms of External Quantum Efficiency (η_{ex}) defined as:

$$\eta_{ex} = Resp\frac{hc}{e\lambda} \tag{3.4}$$

Fig 3.18 shows the η_{ex} for pattern C, single microcrystal, and the

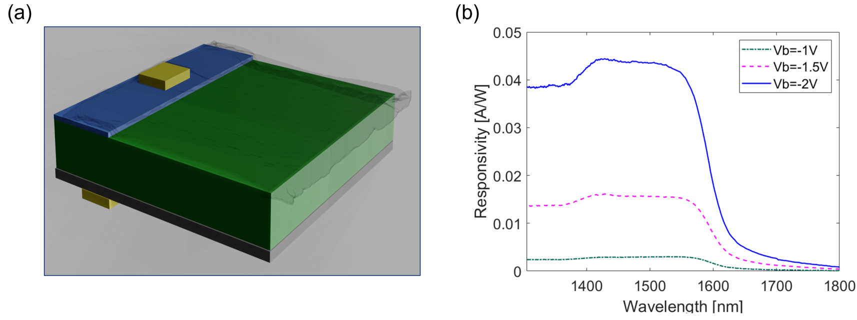

Figure 3.16: (a) Sketch of the Ge planar device; (b) Responsivity of the Ge planar device for three different reverse bias.

graphene/microcrystals array. The fabrication process using graphene as a top contact caused a reduction of approximately 50% of the η_{ex} in the Ge direct regime of absorption

We notice that the responsivities of microcrystal arrays and of the 5μm thick reference photodiode are all much lower than that of conventional Ge-on-Si photodiodes [18], which are typically $\approx 1\mu$m thick. To clarify the role played by the layer thickness we set up a simplified 1D model to estimate the theoretical expected value of the η_{ex}. This 1D model does not take into account the particular morphology of the microcrystal but the thickness of the different doping regions of the *p*-*i*-*n* junction of Ge and the recombination processes that can take place within the structure itself. The simulation are performed by means of a Poisson Drift-Diffusion model implemented in SESAME, a python based library [24].

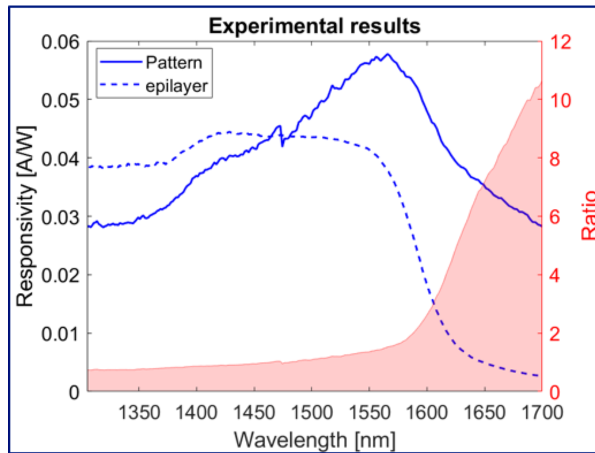

Figure 3.17: Comparison between the responsivity of the graphene/Ge microcrystal device obtained from pattern C (continuous line) and the responsivity of the Ge planar device (dashed line). In both cases the photocurrent has been acquired at -3V. The area in red indicates the ratio between the responsivity of the patterned and planar device.

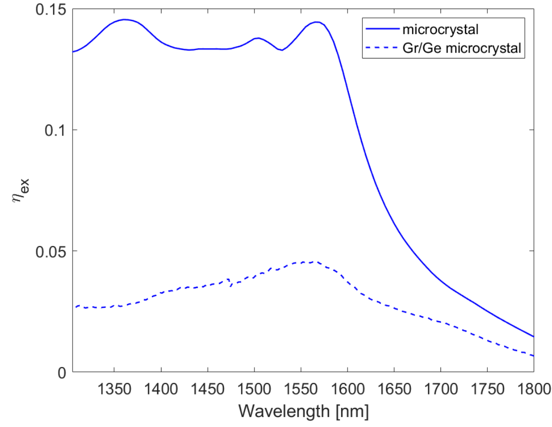

Figure 3.18: Comparison of the η_{ex} of single microcrystal (continuous line) and a graphene/microcrystal array device (dashed line).

The results are given by expressing the thickness of the absorbing layer in terms of the carrier diffusion length in the i-region. The sketch of the simulated structure and the results of the simulation are represented in Fig 3.19. In particular, from Fig 3.19(b) it is possible to note that there is an optimal thickness value of the absorbing layer with respect to the diffusion length that allows a maximization of the η_{ex}. This condition is possible when the absorbing layer has a thickness comparable to the diffusion length. In addition Fig 3.20 shows the η_{ex} as a function of the wavelength for different absorbing layer thicknesses.

In our case the thickness of the intrinsic zone is approximately three times the diffusion length, therefore a strong reduction of the η_{ex} is observed with a value comparable to that obtained experimentally for the Ge microcrystal. This gives a trade-off in choosing the optimal microcrystal thickness.

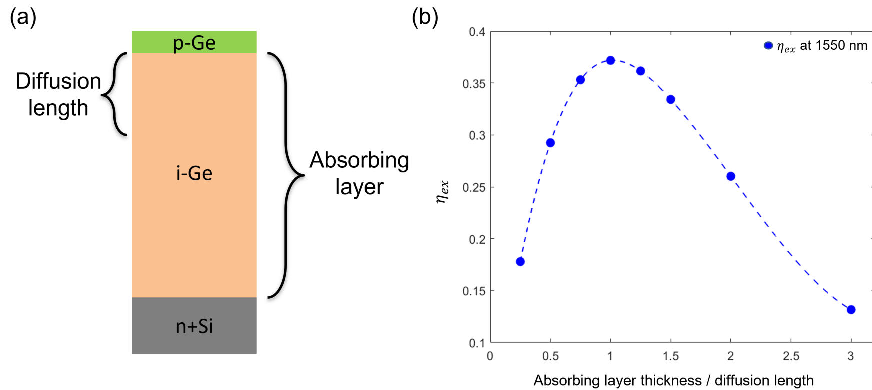

Figure 3.19: (a) Sketch of the Ge p-i-n simulated structure; (b) η_{ex} as a function of the ratio between the absorbing layer thickness and the diffusion length, at 1500 nm.

Thick absorbing layer implies stronger light trapping effects but at the same time increases the carrier recombination rate. A longer diffusion length in the microcrystal as compared with an equivalent planar epilayer is a possible solution to obtain a thicker absorbing layer. This parameter is influenced by the defects present in the material, which can act as recombination centers. As already discussed in 2.3.1 the density of threading dislocations in microcrystal is lower than in conventional epilayers. At the same time, microcrystals feature a larger surface-to-volume ratio compared to an equivalent planar epilayer. Surface passivation of the microcrystal would therefore result in a strong reduction of the recombination and therefore to a longer diffusion length.

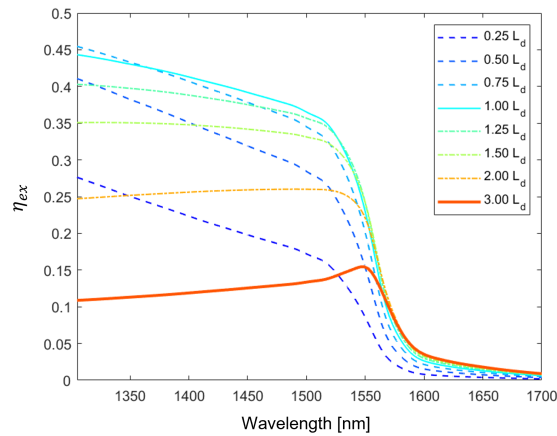

Figure 3.20: Simulation of the η_{ex} in the wavelength range from 1300 to 1700 nm, for different thickness of the absorbing layer.

In conclusion, an optimization of the quality of the material is necessary to obtain a device with an improved η_{ex}.

Chapter 4

Si microcrystals as a photodetection platform

In this chapter we analyze the optical (4.1), electronic (4.2) properties and the photoresponse of silicon microcrystals (4.3). As already discussed in section 1.2, silicon is an excellent semiconductor to fabricate devices not only operating as linear photodetectors but as APD (4.4) or SPAD (4.5) working in the wavelength range between 500 and 1100 nm.

4.1 Optical simulation of Si microcrystals 49
4.2 Electrical properties of Si microcrystals 50
4.3 Electro-optical characterization of a single Si microcrystal 52
4.4 Implanted Si microcrystal as avalanche photodiodes 55
4.5 Implanted Si microcrystal as single photon avalanche diodes 56

4.1 Optical simulation of Si microcrystals

Similarly to what has been done for Ge microcrystals (3.1.1), FDTD simulations have been performed to model the optical properties of Si microcrystals. Also in this case the aim is comparing the optical properties of the particular morphology of the microcrystal with a Si equivalent planar epilayer, characterized by the same refractive index (real and imaginary part). The domains of these new simulations and their results are shown in Fig 4.1.

As can be seen from Fig 4.1(a) we are now in conditions of homo-epitaxy, in which both the patterned pillar and the material grown by LEPECVD are made of silicon. In Fig 4.1(b) the fractions of absorbed power for the pattern and for the equivalent planar epilayer, and their corresponding ratio are presented. An increase in the fraction of absorbed power for the Si microcrystal with respect to the planar equivalent epilayer can be observed. Their ratio will have a sharp increase close to the Si gap. This feature is linked to the light trapping effect that occurs in the microcrystal following the illumination of the inclined top facets,

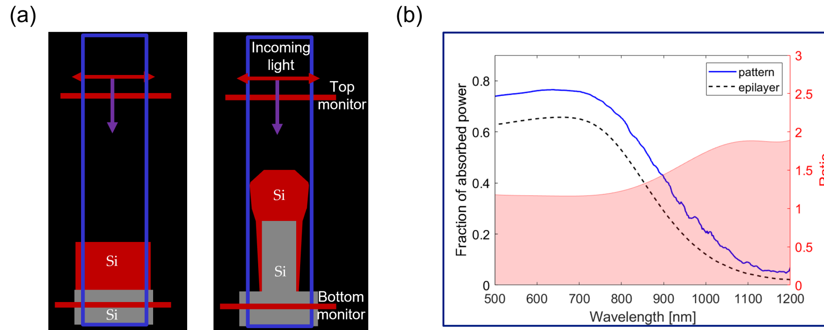

Figure 4.1: (a) Sketches of the simulation domains for a Si planar epilayer and a Si microcrystal; (b) Fraction of absorbed power of the Si pattern (continuous red line) and of the Si planar epilayer (red dashed line). The ratio between these two quantities is represented by the shaded area.

resulting in a longer optical path inside the microcrystal. This phenomenon then allows to have a greater fraction of absorbed power even at wavelengths at which the absorption coefficient of Si is low.

4.2 Electrical properties of Si microcrystals

To use silicon microcrystals as APD or SPAD, an optimization of the doping profile of the microcrystal itself is required. For this reason electronic simulations have been developed by the group of Prof. A. Tosi of the Department of Electronics of the Politecnico di Milano (2.4.1). Two simulated doping profiles are represented in Fig 4.2.

The doped profile of Fig 4.2(a) represents the dopant distribution achievable with an in-situ doping, i.e. performed during the LEPECVD growth of the microcrystals. The doping profile is characterized by a p-type top contact spreading on the sidewalls of the microcrystal. This is due to surface diffusion and shadowing processes which influence the morphology of the deposited material, generating this "shell" doping profile (Fig 4.3(a)). Starting from such doping profile it is possible to calculate the distribution and the absolute value of the electric field inside the microcrystal, and the associated avalanche probability. Due to the faceted surface of the microcrystal close to its edges there are electric field "hot-spots", which lead to edge-breakdowns (Fig 4.3(b)). These electric field "hot spots" imply high avalanche probability near the surface defects (Fig 4.3(c)). This characteristic leads to an anticipated breakdown with respect to the one achievable in a "flat" junction with similar doping levels, with a consequent reduction of the maximum gain M (see section 1.2).

To overcome this problem, another doping profile has been implemented and simulated, in which the last p^+-type top contact was implanted (Fig.4.2(b)). With this profile the doped material and the resulting internal electric field (Fig 4.4(a,b)) is more confined to the center of the microcrystal. This prevents the formation of edge-breakdowns, resulting in a avalanche probability higher away from the surface states of the microcrystal (Fig 4.4(c)).

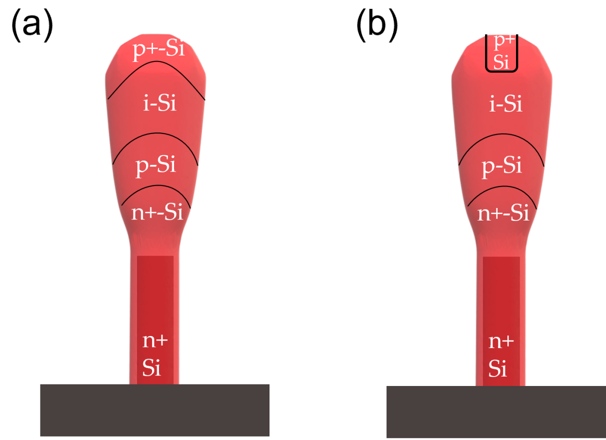

Figure 4.2: (a) Doping profile for an in-situ doped Si microcrystal; (b) Doping profile for an implanted Si microcrystal.

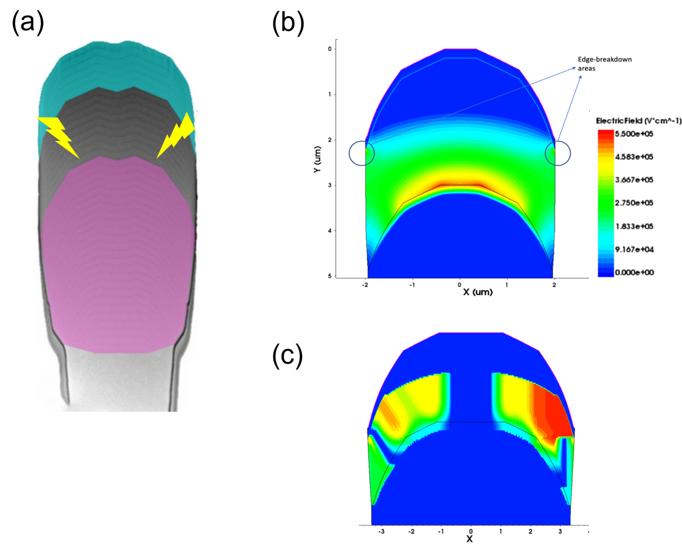

Figure 4.3: (a) Sketch of the shape of the doping profile considering diffusion and shadowing effects; (b) Resulting electric field distribution; (c) Resulting avalanche probability distribution.

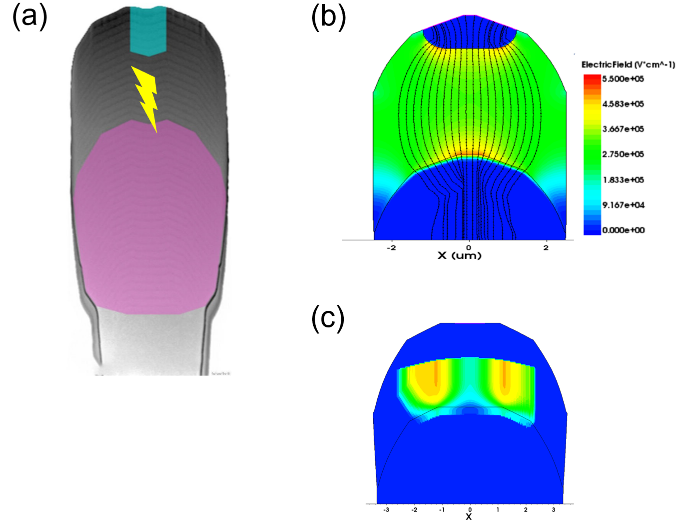

Figure 4.4: (a) Sketch of the doping profile for an implanted microcrystal; (b) Resulting electric field distribution; (c) Resulting avalanche probability distribution.

To experimentally test these two doping profiles, IV curves of single microcrystal have been acquired with the setup described in 3.1.2 consisting of a nanomanipulator, a confocal microscope and a source-meter. The results are shown in Fig 4.5. It can be observed that the IV curve for the in-situ doped presents an anticipated breakdown and a greater dark current due to the high electric field at the edges of the microcrystal. On the other hand, the implanted microcrystal presents a sharper BD and a reduction of the dark current thanks to the better confined distribution of the electric field and of the avalanche probability.

4.3 Electro-optical characterization of a single Si microcrystal

Following the electrical analysis of single Si microcrystals, we characterized their photoresponse. The responsivity measurements were performed using the setup already described, consisting of a confocal microscope and a nanomanipulator (section 3.1.2). A source meter is used to acquire the photocurrent signal. First the dark IV curve is measured. Subsequently, the IV under illumination at different fixed biases, for wavelengths changing between 500 and 1200 nm are acquired. The photocurrent is obtained as the difference between the IV under illumination and the dark current. These measurements were performed for a couple of patterns. In both cases an in-situ doped and implanted microcrystals have been analyzed. The geometric characteristics of these patterns are indicated in Fig 2.6, while the top-view SEM images are shown in Fig 4.6. The analyzed patterns feature different morphologies of the microcrystals: different predominant facets at the top, different shapes and different sizes. In particular

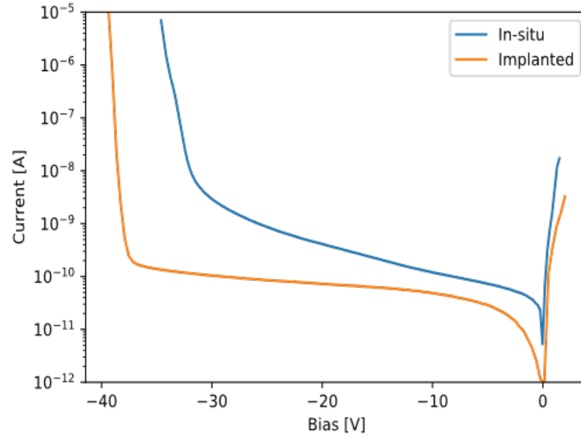

Figure 4.5: IV curve of a single Si microcrystal from pattern K: in-situ doped (blue continuous line) and implanted (orange continuous line).

pattern K is predominantly faceted, while pattern N is a predominantly flat microcrystal (see Fig 2.7). The responsivity measured for these two patterns both for the in-situ doped and for the implanted one are represented in Fig 4.7. In both cases the responsivity for the in-situ doped microcrystal is slightly greater than that of the implanted one. This is particularly true at longer wavelengths i.e. close to the Si energy gap. In an equivalent way to what has already been done for Ge microcrystals, the photoresponse of microcrystals has been compared with that of an equivalent Si mesa diode. The latter is fabricated by means of laser writer and RIE, such as to have a width equal to that of the microcrystals pattern, i.e., 100 μm (Fig 4.8(a)). The photoresponse of the mesa diode is acquired using the nanomanipulator and the confocal microscope setup. (Fig 4.8(b)). By comparing the responsivity obtained for the planar device with that of the microcrystal, we can note that the in-situ doped microcrystal presents an enhancement of the responsivity in the NIR, with respect to the mesa diode, (Fig 4.9(a,b)) greater than that which can be achieved for the analogous implanted

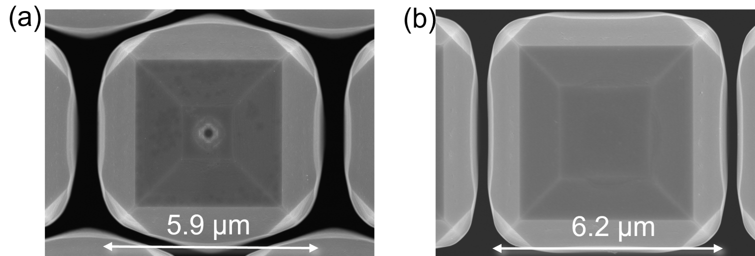

Figure 4.6: Top-view SEM images of pattern K, predominantly faceted (a), and pattern N, predominantly flat (b).

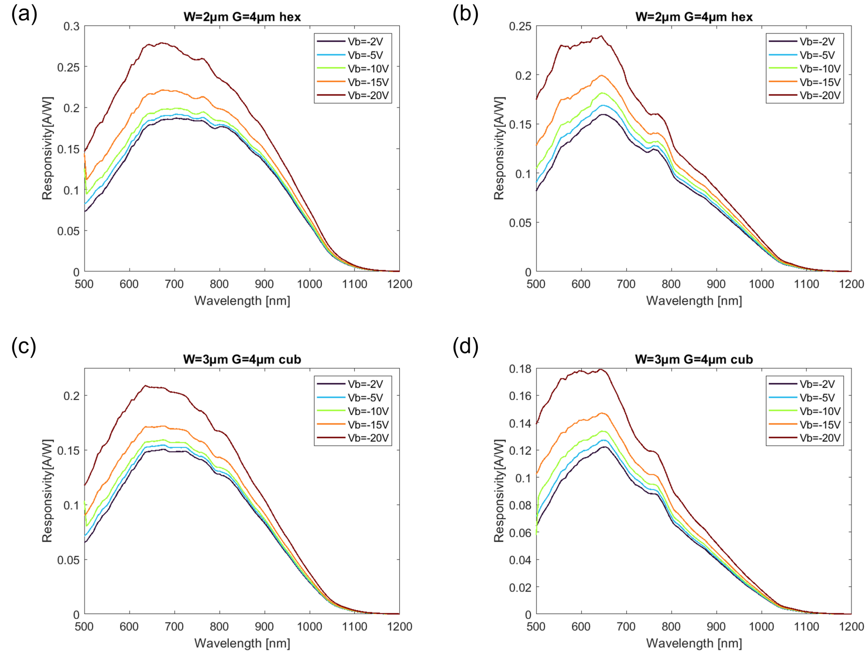

Figure 4.7: Responsivity for different bias between -2V and -20V for pattern K and N: (a) K in-situ doped, (b) K implanted, (c) N in-situ doped and (d) N implanted.

microcrystal (Fig 4.9(c,d)). This higher enhancement of the responsivity in the NIR, of the in-situ doped microcrystal, is linked to the "shell" doping profile that yields a larger collection volume of the photogenerated electrons with respect to the implanted case. Furthermore, it can be noted that this increase in the responsivity in the NIR is greater for the microcrystal predominantly faceted (K) than for the predominantly flat (N). This effect is linked to the greater

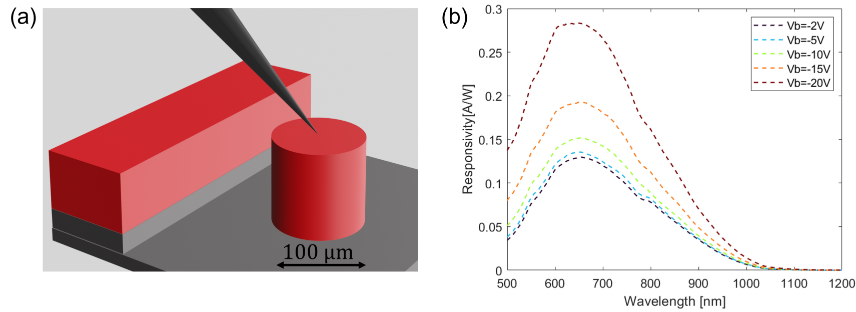

Figure 4.8: (a) Sketch of the Si mesa diode, fabricated by optical lithography and RIE. The tip of the nanomanipulator is used as top contact. (b) Responsivity of the Si mesa diode for reverse bias between -2V to -20V.

faceting of the microcrystal K, yielding an increase in the light trapping effect resulting in a greater absorption also at longer wavelengths. This feature makes the in-situ doped microcrystals optimal for fabricating Si devices with higher NIR responsivity. The implanted microcrystals will be the optimal choice for APDs and SPADs, thanks to their low dark current and a sharp breakdown.

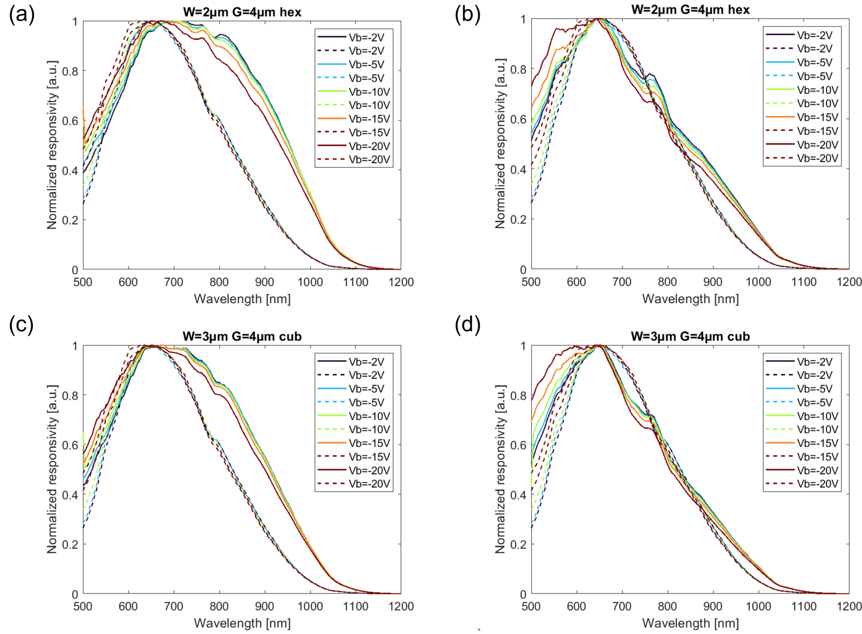

Figure 4.9: Comparison between the normalized responsivities of the microcrystals and the fabricated Si mesa-diode: (a) K in-situ doped (continuous lines) and mesa-diode (dashed lines), (b) K implanted (continuous lines) and mesa-diode (dashed lines), (c) N in-situ doped (continuous lines) and mesa-diode (dashed lines) and (d) N implanted (continuous lines) and mesa-diode (dashed lines).

4.4 Implanted Si microcrystal as avalanche photodiodes

The implanted microcrystals have the optimal electrical characteristics to operate as APD. As seen in section 1.2, a fundamental parameter to define the performance of an APD is its gain. To measure the latter it is necessary to operate under conditions of low incident power on the sample. For this reason, the photocurrent has been acquired using the same setup described in section 3.1.2, with the addition of a Neutral Density filter (ND), placed between the laser source and the beam splitter, with density equal to 6.1 resulting in a final power incident on the sample of a few nW. Once the photocurrent curves as a function of the applied voltage are acquired for four fixed wavelengths: 700, 800, 900 and 1000 nm, we calculated the gain M(V) using the formula (1.12). The reference voltage V_0 chosen is -3V, far from the breakdown voltage of the

junction which is around -38V. The experimental gains obtained, both for the microcrystal of the K and N pattern, are represented in Fig 4.10.

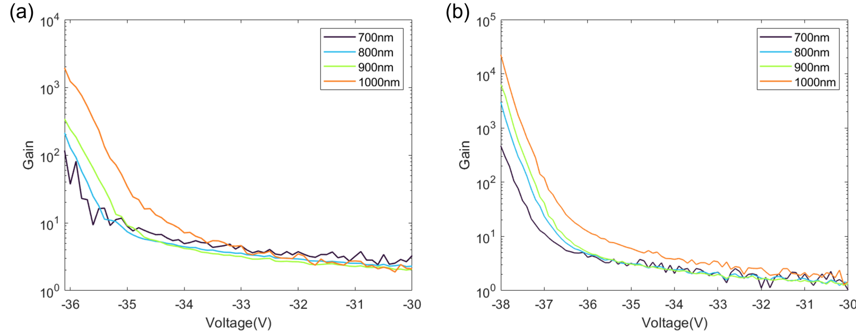

Figure 4.10: Experimental gain M(V) for four different wavelengths 700, 800, 900 and 1000 nm: (a) Pattern K; (b) Pattern N.

Pattern N, predominantly flat, presents a gain higher than pattern K, predominantly faceted. By comparing the gain obtained for the different wavelengths, for each pattern, it can be observed that there is higher gain at longer wavelengths. This phenomena is linked to the fact that longer wavelengths are absorbed closer to the multiplication region, and so more electron-hole pairs generated will trigger an avalanche. Furthermore, the experimental gain M(V) has a maximum value between 10^2 and 10^4, therefore comparable to the gain of state-of-the-art CMOS APD [25].

We decided to continue the analysis for the predominantly flat pattern N, that has a higher gain, comparing its experimental gain with the fittings obtained with the semi-empirical method. To fit the experimental gain M(V) for the four different wavelengths, we look for the minimum of the least squared of the transcendental equation (1.15) while keeping n and V_{BD} as free parameters and setting $I_{d0} = 1 \times 10^{-10}$A and $R = 900$KΩ from the dark IV curve and I_{ph0} from the illuminated ones. The value of R has been extrapolated from a linear fit of the forward region of the dark IV curve. Fig 4.11 shows the results achieved for the four wavelengths. It can be observed how the theoretical model fits very well the experimental data for almost the entire voltage range.

4.5 Implanted Si microcrystal as single photon avalanche diodes

The working principle of a single photon avalanche diode has already been summarized in section 1.3. To test whether the implanted Si microcrystal can operate not only as an APD but also as a SPAD, it is necessary to perform measurements on a fully fabricated device, i.e. one featuring contacts that can be bonded to an external read-out circuit without the use of the nanoprobe. At variance with the Ge microcrystal device, we decided not to use graphene as a top contact due to the poor reproducibility of the transfer step. Instead, new fabrication strategies have been attempted.

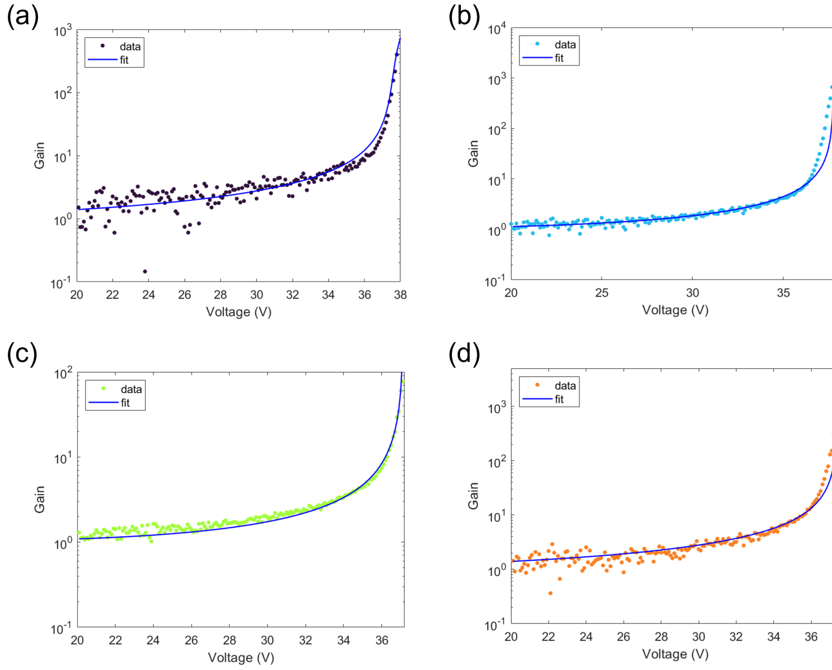

Figure 4.11: Comparison between the experimental gain of pattern N and the fitting obtained by the semi-empirical equation (1.15) for the four wavelengths: (a) 700 nm, (b) 800 nm, (c) 900 nm and (d) 1000 nm.

The first fabrication process have been developed at the Politecnico di Milano, and is based on photoresist filling and on the use of Indium Tin Oxide (ITO) as top transparent contact. To achieve a continuous layer of ITO on the patterned region, a process for filling the gaps between the microcrystals has been developed. The sketch of each step of this fabrication process are represented in Fig 4.12. The initial state of the sample is that after PECVD SiO_2 deposition and the removal of the latter from the patterned area by means of optical lithography and HF wet etch (Fig 4.12(a)). In the first step the photoresist AZ5214 is spin coated on the sample. The recipe used for this process is based on spinning at a speed of 6000 rpm with an acceleration of 500 rpm/s for 60 s. Before exposure the sample is backed on a hot plate at 110°C for 90 s.

The second step is the exposure by laser writer of the photoresist spinned on the patterned area. For this exposure we used a reduced dose, 20% of the nominal dose of 230 mJ/cm^2. In this way, after the development with AZ726 developer for 60 s, the photoresist is not completely removed from the patterned area but only the top of the microcrystals has been uncovered (Fig 4.12(b)).

The third step is another exposure with 100% of the nominal dose in order to completely remove the photoresist from the unpatterned region (Fig 4.12(c)). The sample is thus ready for the last step, the sputtering of 200 nm of ITO (Fig 4.12(d)).

Fig 4.13(a) shows the top-view SEM image of the sample after the photoresist

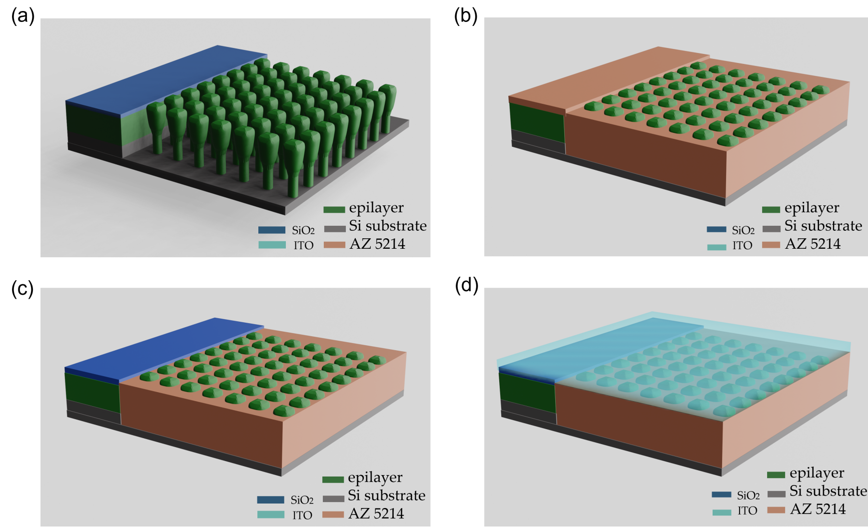

Figure 4.12: Sketches of the fabrication steps based on photoresist filling and ITO as top transparent contact: (a) starting state of the sample, with SiO_2 just on the unpatterned region; (b) sample after the first laser writer exposure to uncover the top of the microcrystals; (c) sample after the second laser writer exposure to remove all the photoresist on the unpatterned region; (d) ITO sputtering deposition.

filling process. The bright area on the top of the microcrystal is the photoresist-free region. It can be seen how the photoresist is able to fill the gap between the microcrystals, and to form a "bridge" between them and between the patterned and unpatterned area. Fig 4.13(b) shows the top-view SEM image after the sputtering deposition of ITO.

After the development of this fabrication process, we analyzed the IV curve

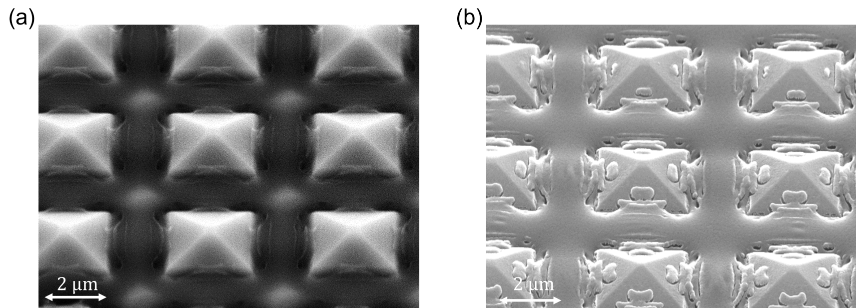

Figure 4.13: (a) Top-view SEM image of the microcrystal array after photoresist filling process; (b) Top-view SEM image after the 200 nm ITO sputtering deposition. ITO covers all the patterned region, the top of the microcrystals and photoresist between them.

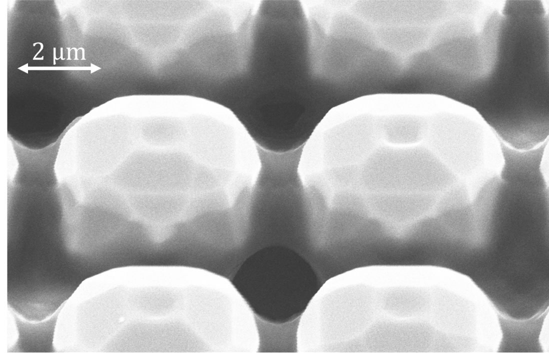

Figure 4.14: SEM image of the pattern after the photoresist filling process. The photoresist fills the gap between the microcrystals, generating bridges between them. Despite that in some region of the pattern holes are present between microcrystals.

of the final device to test the junction generated at the interface between the ITO and the p^+-type top of the microcrystal. The IV curve, acquired by means of the nanomanipulator and source-meter didn't show the expected rectifying behaviour making this fabrication process unsuitable for applications as APD or SPAD. This is most likely due to the ITO penetrating the holes in the photoresist forming during the filling process (Fig 4.14) and contacting the microcrystal sidewalls.

An alternative fabrication process has been developed at the University of Glasgow, by the team of Prof. D. Paul. This fabrication process is based on SiO_2 deposition and planarization, with the use of a metal as top contact. The steps of this process are represented in Fig 4.15 and are described here below:

1. Passivation of the lateral surfaces of the microcrystals by means of thermal SiO_2 deposition (Fig.4.15(a)).
2. PECVD deposition of 10 μm of SiO_2.
3. Chemical-Mechanical Polishing (CMP) to reduce the thickness of the SiO_2 above the microcrystals.
4. First step of EBL and HF wet etch to uncover just the top of the microcrystals (Fig.4.15(b)).
5. Second step of EBL to allow the evaporation of a metal contacting the top of a single or few microcrystals (Fig.4.15(c)). The mask used for the lithographic process made it possible to contact both single microcrystals and arrays (Fig.4.15(d)).

Fig 4.16 shows the dark and illuminated IV curves obtained after this fabrication process, measured at 100 K. The dark IV curve has the desired shape, characterized by a low dark current and a sharp breakdown. The illuminated IV curve confirms the photoresponse of the final device. The use of the metal as top contact, strongly reduces the light absorbed by the microcrystals. This phenomena leads to a reduction of the final responsivity of the fabricated device,

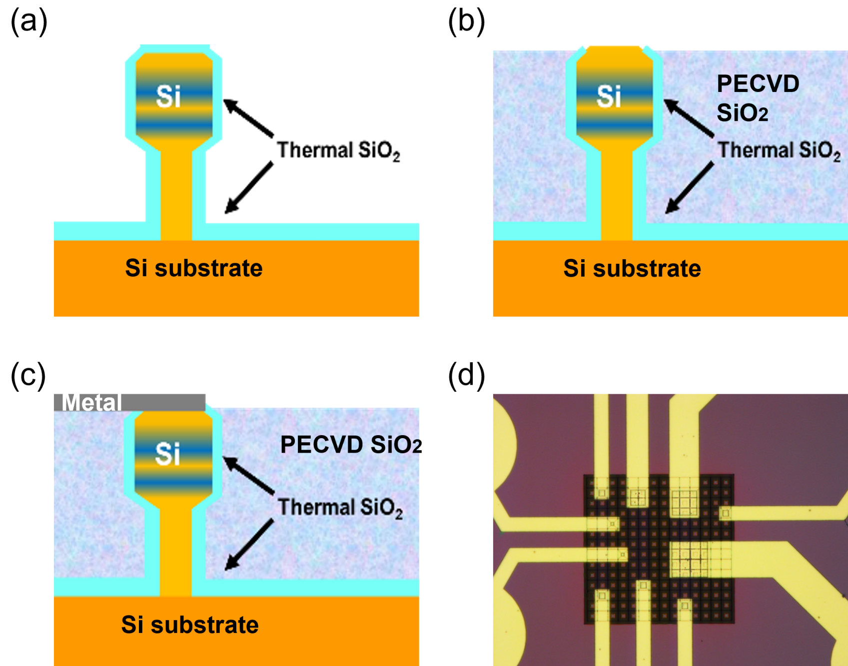

Figure 4.15: Sketches of the fabrication process based on SiO_2 deposition and planarization, and metal as top contact. (a) surface passivation by thermal SiO_2; (b) PECVD deposition of SiO_2 and CMP with HF wet etch to uncover the top of the microcrystal; (c) evaporation of the metal contact; (d) optical microscope image of the final device.

with a maximum value of 6×10^{-2} A/W. For this reason we decided to fabricate another device with all the fabrication steps identical to those described above, except for the top contact which was obtained by the sputtering of 200 nm of ITO. The dark and illuminated IV curves at 300 K and 100 K measured after this fabrication process, are represented in Fig 4.17. The breakdown is observed but it is not sharp, and there is an increase of the dark current respect with the value obtained for the device with metal as top contact (Fig 4.16) confirming the poor electrical properties of the ITO-Si contact.

Despite this non ideal IV curve we still tried to characterize the photoresponse of this ITO device by using the setup described in section 3.1.2. The responsivity obtained has its maximum value almost equal to 0.2 A/W at the bias -7V, and the comparison with the responsivity of the metal device is shown in Fig 4.18. It can be noted that the responsivity of the device with ITO top contact is more than an order of magnitude higher than that one with the metal contact.

Despite the reduction of the responsivity of the metal device, we decided to test its application as SPAD. These measurements have been made by the group of Prof. A. Tosi at the Electronic Department of the Politecnico di Milano. The analysis in the avalanche regime of the metal/Si microcrystal have been made in

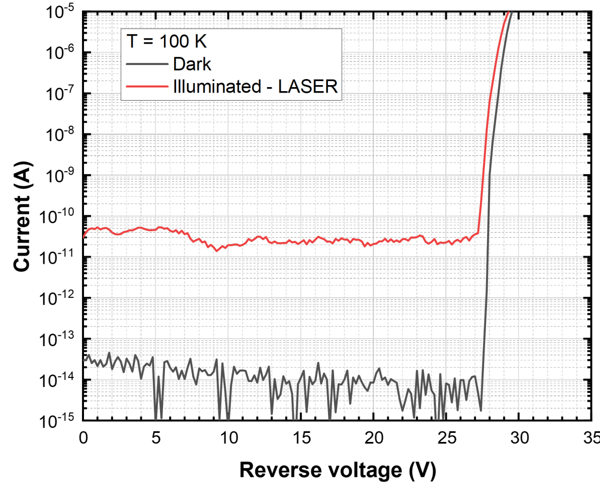

Figure 4.16: Dark (black continuous line) and illuminated (red continuous line) IV curve of the metal device based on Si microcrystals, acquired at 100 K.

gated-mode operation (Fig 1.7). For these measurements the sample is placed in a cryostat at a temperature of 100 K and a pressure of 10^{-4} mbar. The ON-TIME used was 50 ns, while the OFF-TIME was of the order of μs to avoid after-pulsing. In this way, during the gate-on timespan a single photon can trigger an avalanche pulse. During the gate-off timespan the device is not sensitive to the incoming photon flux. It is possible to measure in real time the response of the device by means of an oscilloscope. Fig 4.19(a) shows the response obtained under dark condition. It is present a peak of current linked to the gate opening and closing, and an avalanche pulse generated by a dark count. Fig 4.19(b) shows the oscilloscope trace under illumination. The presence of different avalanche pulses confirms the photoresponse of the SPAD. In the dark condition the dark count rate (DCR) of the SPAD can be measured. For the Si microcrystals a value of 10^3 Count Per Second (cps) at a temperature of 100 K has been obtained. This value is far from the literature best dark count rate of a SPAD which is typically around 10 cps at room temperature. High DCR are typically associated to a high density of defects such as vacancies or surface states. A reduction of the DCR would then require an optimization of the microcrystal growth and surface passivation.

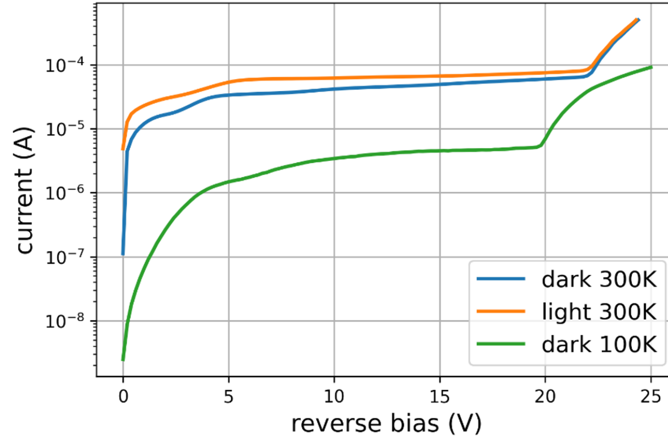

Figure 4.17: Dark (blue continuous line for 300 K, green continuous line for 100 K) and illuminated (orange continuous line for 300 K) IV curve of the ITO device based on Si microcrystals.

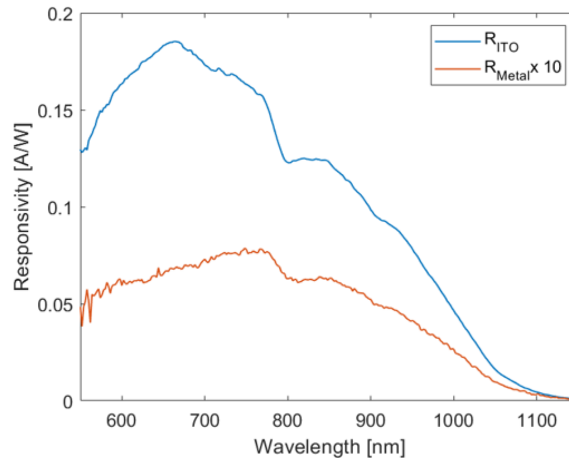

Figure 4.18: Comparison between the responsivity of the ITO device (blue continuous line) and the metal one (orange continuous line) for a bias of -7V. The responsivity of the device with ITO as top contact has a responsivity more than an order of magnitude larger than that of the device with the metal contact.

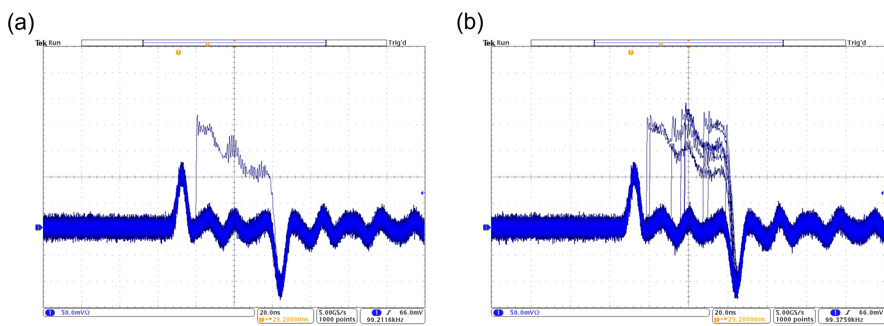

Figure 4.19: Real time response of the metal device operating in gated-mode. (a) oscilloscope trace under dark condition; (b) oscilloscope trace under illumination that confirms the photoresponse of the device.

Conclusion

In this thesis I have presented the development of a novel class of photodetectors operating in the VIS-SWIR region. The building blocks of such photodetectors are 3D self-assembled microcrystals, made of Si/Si (absorption from 500 up to 1200 nm) or Ge/Si (absorption from 1200 up to 1800 nm). I have shown the simulation, fabrication and characterization of this microcrystal-based photodetectors.

First, the electronic properties have been modelled by TCAD simulations. In this way the optimal doping profile required to achieve the desired distribution of the electric field inside the microcrystal has been estimated. Then, I computed the optical properties of the microcrystals by FDTD simulations. From the latter it is clear that the microcrystals feature a higher fraction of absorbed power compared to an equivalent planar epilayer. In particular, for a Ge/Si microcrystal this enhancement is more pronounced in the indirect regime of absorption of Ge. Even though to a lower extent, also in the Si/Si case the microcrystals absorb more light when compared with an equivalent epilayer.

To experimentally demonstrate such interesting properties we proceed first with the characterization of single Ge/Si and Si/Si microcrystals and then with the fabrication and characterization of the devices exploiting microcrystal arrays. In particular, the Ge/Si microcrystals device and the equivalent planar epilayer have been fabricated by the use of a double-layer of graphene as top transparent contact. In this way, it was possible to obtain a continuous top contact that can adapt to the 3D morphology of the microcrystals.

The responsivity measured for a single Ge/Si microcrystal and that of the graphene/Ge photodetectors, confirmed the trend predicted by the FDTD simulations. Indeed, an enhancement of the responsivity for the microcrystals in the indirect regime of absorption of Ge (over 1550 nm) as been observed, with respect to the Ge equivalent planar epilayer.

In the case of Si microcrystals two different doping strategies have been investigated: in-situ doping and implantation. The in-situ doped microcrystal features a larger collection volume, leading to a higher responsivity. The implanted Si microcrystal has an optimal IV curve, characterized by a sharp breakdown and a low dark current. For this reason, the possibility of using the implanted Si microcrystals not only as a linear photodetector but also as an APD and SPAD has been investigated. The measurements performed on the implanted Si microcrystals in the avalanche regime confirmed the possibility to use them as APD, with a maximum gain comparable to the state of art. Two fabrication processes have been developed to fabricate a device based on implanted Si microcrystals that can operate as a SPAD. The one based on the SiO_2 deposition and planarization and the metal contact guaranteed a rectify-

ing behaviour of the final IV curve of the device. Gated-mode measurements confirmed the possibility to employ the microcrystals for the detection of single photon, even though further material optimization is required to reduce the dark count rate.

In conclusion we demonstrated the possibility to exploit Si and Ge microcrystals as VIS-SWIR photodetectors also operating as APDs and SPADs.

Appendix A

Additional data

A.1 FDTD simulations of Ge/Si microcrystal

In section 3.1.1 we saw the results of the FDTD simulations for the three pattern A, C, O and for the Ge planar epilayer (Fig 3.3). The three pattern feature a larger fraction of absorbed power respect the planar epilayer. In particular in Fig 3.4 a stronger enhancement of the fraction of absorbed power of the pattern C, with respect to the epilayer, is visible in the indirect regime of absorption. This trend is supported also by the modelling of pattern A and O. Fig A.1(a) shows the fraction of the absorbed power for pattern A and for the Ge planar epilayer and the corresponding ratio. Similar data for pattern O are shown in Fig A.1(b).

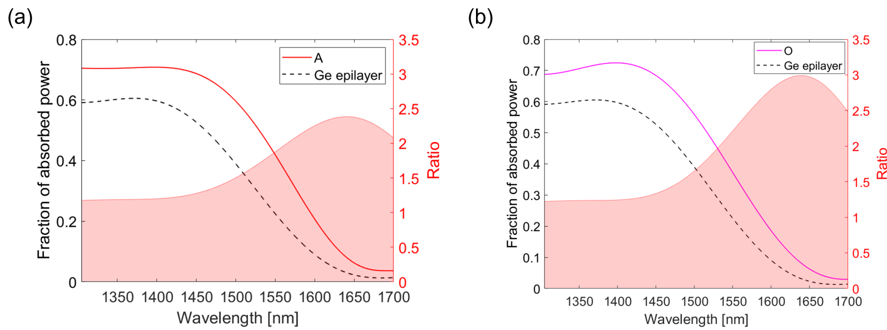

Figure A.1: Ratio between the fraction of absorbed power of the pattern A,O and the Ge planar epilayer: (a) pattern A; (b) pattern O.

These results confirm the property of the Ge/Si microcrystals to enhance the absorption of the incident light, by light trapping effect, in the indirect regime of Ge absorption.

A.2 Responsivity dependence on morphology for single Ge/Si microcrystal

The setup used for the electro-optical characterization of a single microcrystal, based on a confocal microscope and a nanomanipulator has already been described in section 3.1.2. The characterization of single microcrystals evidenced a clear dependence of responsivity on morphology. In detail in Fig 3.8 we observe that the responsivity of the predominantly faceted microcrystal G, above 1550 nm, is larger when compared to that of the predominantly flat pattern O. To generalize this trend observed for patterns G and O, we also carried out the same type of measurement for two other patterns C and I. The geometric characteristics of those pattern and their degree of faceting, calculated by the equation (2.1), are shown in Fig A.2.

Pattern	W (μm)	G (μm)	CONF.	Dfac[%]
C	2	4	cub	99.2
I	3	3	cub	87

Figure A.2: Geometric characteristics and degree of faceting for patterns C and I.

The normalized responsivity obtained for these two patterns (see Fig A.3) confirms the trend observed in Fig 3.8. The responsivity of pattern C, predominantly faceted as G, is larger than the responsivity of pattern I, predominantly flat as O.

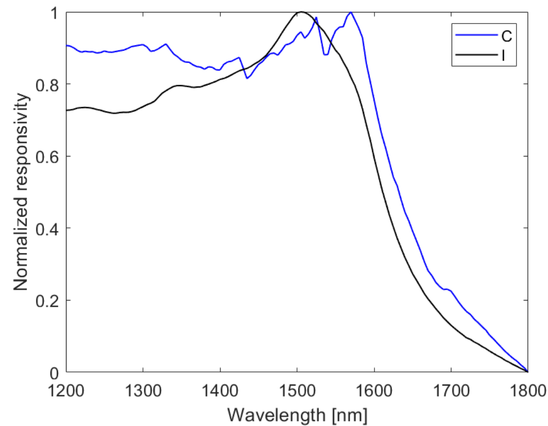

Figure A.3: Normalized responsivity of the pattern C, predominantly faceted, and of pattern I, predominantly flat.

A.3 NEP and specific detectivity of implanted Si microcrystal

In the section 1.1 the NEP and D^* of a photodetector have been defined. To better quantify the performances of the in-situ doped and implanted Si microcrystals, we calculated the NEP and D^* by using Eq. (1.8) and Eq. (1.9) for the reverse bias of -5V. Fig A.4 shown the obtained NEP and D^* for the microcrystals, in-situ doped and implanted, K and N.

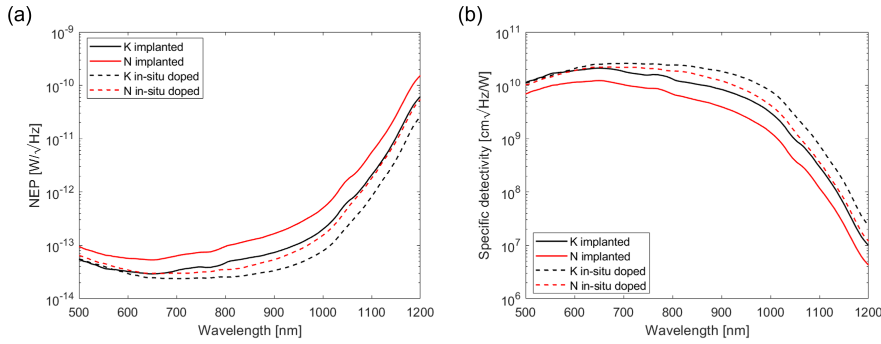

Figure A.4: (a) NEP of the in-situ doped and implanted Si microcrystals K and N; (b) D^* of the in-situ doped and implanted Si microcrystals K and N.

The NEP has a minimum for the K in-situ doped microcrystal at $2.8 \times 10^{-14}\text{W}/\sqrt(\text{Hz})$ at 850 nm. It is of the same order of magnitude of the NEP of the FDS025 - Si Thorlabs photodiode equal to $1 \times 10^{-14}\text{W}/\sqrt{\text{Hz}}$ at the same wavelength and bias.

Instead the specific detectivity of the Si thorlabs photodiode, is almost equal to $2.21 \times 10^{12}(\text{cm} \times \sqrt{\text{Hz}})/\text{W}$. The latter is two order of magnitude larger than the maximum detectivity obtained for the K in-situ doped microcrystal $(2.18 \times 10^{10}(\text{cm} \times \sqrt{\text{Hz}})/\text{W})$. More optimization of the material and its surfaces are required to reach a higher detectivity.

Bibliography

[1] J. Michel, J. Liu, and L. Kimerling. High-performance Ge-on-Si Photodetectors. *Nature Photonics* **4**, 527 (2010).

[2] C. Falub, H. von Känel, F. Isa, R. Bergamaschini, A. Marzegalli, D. Chrastina, G. Isella, E. Müller, P. Niedermann, and L. Miglio. Scaling Hetero-Epitaxy from Layers to Three-Dimensional Crystals. *Science (New York, N.Y.)* **335**, 1330 (2012).

[3] R. Bergamaschini, F. Isa, C. Falub, P. Niedermann, E. Müller, G. Isella, H. von Känel, and L. Miglio. Self-aligned Ge and SiGe three-dimensional epitaxy on dense Si pillar arrays. *Surface Science Reports* **68**, 390 (2013).

[4] J. Pedrini, P. Biagioni, A. Ballabio, A. Barzaghi, M. Bonzi, E. Bonera, G. Isella, and F. Pezzoli. Broadband control of the optical properties of semiconductors through site-controlled self-assembly of microcrystals. *Opt. Express* **28**, 24981 (2020).

[5] V. Falcone, A. Ballabio, A. Barzaghi, C. Zucchetti, L. Anzi, F. Bottegoni, J. Frigerio, R. Sordan, P. Biagioni, and G. Isella. Graphene/Ge microcrystal photodetectors with enhanced infrared responsivity. *APL Photonics* **7**, 046106 (2022).

[6] S. Sze and K. K. Ng. *Physics of Semiconductor Devices*. John Wiley & Sons, Ltd (2006).

[7] L. K. Anderson and B. J. McMurtry. High-Speed Photodetectors. *Appl. Opt.* **5**, 1573 (1966).

[8] K. G. McKay and K. B. McAfee. Electron Multiplication in Silicon and Germanium. *Phys. Rev.* **91**, 1079 (1953).

[9] R. B. Emmons. Avalanche-Photodiode Frequency Response. *Journal of Applied Physics* **38**, 3705 (1967).

[10] S. Sze and G. Gibbons. Effect of junction curvature on breakdown voltage in semiconductors. *Solid-State Electronics* **9**, 831 (1966).

[11] S. L. Miller. Avalanche Breakdown in Germanium. *Phys. Rev.* **99**, 1234 (1955).

[12] W. G. Oldham, R. R. Samuelson, and P. Antognetti. Triggering phenomena in avalanche diodes. *IEEE Transactions on Electron Devices* **19**, 1056 (1972).

[13] J. E. Ayers, T. Kujofsa, P. Rago, and J. E. Raphael. *Heteroepitaxial Growth*, chapter 3. CRC Press (2016).

[14] C. Rosenblad, H. R. Deller, A. Dommann, T. Meyer, P. Schroeter, and H. von Känel. Silicon epitaxy by low-energy plasma enhanced chemical vapor deposition. *Journal of Vacuum Science & Technology A* **16**, 2785 (1998).

[15] M. Kummer, C. Rosenblad, A. Dommann, T. Hackbarth, G. Höck, M. Zeuner, E. Müller, and H. von Känel. Low energy plasma enhanced chemical vapor deposition. *Materials Science and Engineering: B* **89**, 288 (2002).

[16] H. E. Buckley. Crystal Growth. *Acta Crystallographica* **4**, 384 (1951).

[17] O. Skibitzki, G. Capellini, Y. Yamamoto, P. Zaumseil, M. A. Schubert, T. Schroeder, A. Ballabio, R. Bergamaschini, M. Salvalaglio, L. Miglio, and F. Montalenti. Reduced-Pressure Chemical Vapor Deposition Growth of Isolated Ge Crystals and Suspended Layers on Micrometric Si Pillars. *ACS Applied Materials & Interfaces* **8**, 26374 (2016).

[18] C. Masini, L. Calace, G. Assanto, H.-C. Luan, and L. Kimerling. High-performance p-i-n Ge on Si photodetectors for the near infrared: from model to demonstration. *IEEE Transactions on Electron Devices* **48**, 1092 (2001).

[19] T. Kreiliger, C. V. Falub, A. G. Taboada, F. Isa, S. Cecchi, R. Kaufmann, P. Niedermann, A. Pezous, S. Mouaziz, A. Dommann, G. Isella, and H. von KÃ¤nel. Individual heterojunctions of 3D germanium crystals on silicon CMOS for monolithically integrated X-ray detector. *physica status solidi (a)* **211**, 131 (2014).

[20] G. Isella, J. Osmond, M. Kummer, R. Kaufmann, and H. von KÃ¤nel. Heterojunction photodiodes fabricated from Ge/Si (100) layers grown by low-energy plasma-enhanced CVD. *Semiconductor Science and Technology* **22**, S26 (2006).

[21] R. R. Nair, P. Blake, A. N. Grigorenko, K. S. Novoselov, T. J. Booth, T. Stauber, N. M. R. Peres, and A. K. Geim. Fine Structure Constant Defines Visual Transparency of Graphene. *Science* **320**, 1308 (2008).

[22] L. A. Falkovsky. Optical properties of graphene. *Journal of Physics: Conference Series* **129**, 012004 (2008).

[23] J. Suk, A. Kitt, C. Magnuson, Y. Hao, S. Ahmed, J. An, A. Swan, B. Goldberg, and R. Ruoff. Transfer of CVD-grown monolayer graphene onto arbitrary substrates. *ACS Nano* **5**, 6916 (2011).

[24] B. Gaury, Y. Sun, P. Bermel, and P. M. Haney. Sesame: A 2-dimensional solar cell modeling tool. *Solar Energy Materials and Solar Cells* **198**, 53 (2019).

[25] M.-J. Lee and W.-Y. Choi. A silicon avalanche photodetector fabricated with standard CMOS technology with over 1 THz gain-bandwidth product. *Opt. Express* **18**, 24189 (2010).